Transition to turbulence in quasi-two-dimensional MHD flow driven by lateral walls

Christopher J. Camobreco [ORCID],[1,*] Alban Pothérat [ORCID],[2,†] and Gregory J. Sheard [ORCID][1,‡]

[1]*Department of Mechanical and Aerospace Engineering, Monash University, Victoria 3800, Australia*
[2]*Fluid and Complex Systems Research Centre, Coventry University, Coventry CV15FB, United Kingdom*

This work investigates the mechanisms that underlie transitions to turbulence in a three-dimensional domain in which the variation of flow quantities in the out-of-plane direction is much weaker than any in-plane variation. This is achieved using a model for the quasi-two-dimensional magnetohydrodynamic flow in a duct with moving lateral walls and an orthogonal magnetic field, where three dimensionality persists only in regions of asymptotically small thickness. In this environment, conventional subcritical routes to turbulence, which are highly three dimensional (with large variations from nonzero out-of-plane wave numbers), are prohibited. To elucidate the remaining mechanisms involved in quasi-two-dimensional turbulent transitions, the magnetic field strength and degree of antisymmetry in the base flow are varied, the latter via the relative motion of the lateral duct walls. Introduction of any amount of antisymmetry to the base flow drives the critical Reynolds number infinite, as the Tollmien-Schlichting instabilities take on opposite signs of rotation and destructively interfere. However, an increasing magnetic field strength isolates the instabilities, which, without interaction, permits finite critical Reynolds numbers. The transient growth obtained by similar Tollmien-Schlichting wave perturbations only mildly depends on the base flow, with negligible differences in growth rate for friction parameters $H \gtrsim 30$. Weakly nonlinear analysis determines the local bifurcation type, which is always subcritical at the critical point, and along the entire neutral curve just before the magnetic field strength becomes too low to maintain finite critical Reynolds numbers. Direct numerical simulations, initiated with random noise, indicate that a subcritical bifurcation is difficult to achieve in practice, with only supercritical behavior observed. For $H \leqslant 1$, supercritical exponential growth leads to saturation but not turbulence. For higher $3 \leqslant H \leqslant 10$, a turbulent transition occurs and is maintained at $H = 10$. For $H \geqslant 30$, the turbulent transition still occurs, but is short lived, as the turbulent state quickly collapses. In addition, for $H \geqslant 3$, an inertial subrange is identified, with the perturbation energy exhibiting a $-5/3$ power law dependence on wave number.

I. INTRODUCTION

This work is concerned with the mechanisms that underpin transitions to turbulence in quasi-two-dimensional (Q2D) shear flows, specifically, flow in a rectangular duct pervaded by a transverse magnetic field. A number of natural and industrial flows exhibit quasi-two-dimensional dynamics, where departures from two dimensionality are either asymptotically small in amplitude or only

---

*christopher.camobreco@monash.edu
†alban.potherat@coventry.ac.uk
‡greg.sheard@monash.edu

occur in regions of asymptotically small thickness (for example, boundary layers). This invariably raises the challenge of understanding the appearance of turbulence. In the context of magnetohydro-dynamics (MHD), motivation arises from the search for an efficient design of liquid metal cooling blankets, which extract heat from the adjacent plasma in proposed nuclear fusion reactors [1]. The strength of the plasma-confining magnetic field, which extends into the adjacent blanket ducts, makes the flow there mostly quasi-two-dimensional. Furthermore, turbulence is rapidly damped via the Lorentz force [2]. Though less pertinent to this problem, a second motivation to study Q2D MHD flows has been their remarkable ability to reproduce at laboratory scale the main features of two-dimensional turbulence observed in shallow channel and atmospheric flows [3–5].

Two- or quasi-two-dimensional MHD turbulence was first encountered as a limit state of three-dimensional MHD turbulence at low magnetic Reynolds number [6–8] in domains where out-of-plane boundaries were respectively periodic and no slip. In this limit, the induced magnetic field can be neglected [9], and predominantly the Lorentz force diffuses momentum along the magnetic field lines [10]. When the Lorentz force dominates both diffusive and inertial forces (in the ratios Ha^{-2} and N^{-1}, respectively, where Ha and N are the Hartmann number and interaction parameter), the flow becomes two- or quasi-two-dimensional depending on the boundary conditions [11–14]. Along walls perpendicular to magnetic field lines, viscous forces oppose momentum diffusion by the Lorentz force, forming Hartmann boundary layers of thickness $\approx Ha^{-1}$ [10,15]. A cutoff length scale $l_{\perp}^c \sim N^{2/3}$ separates the larger Q2D scales from the smaller 3D ones [10,16]. However, this cutoff scale cannot drop below that of horizontal viscous friction, so boundary layers parallel to the magnetic field, of thickness $\approx Ha^{-1/2}$, remain intrinsically three-dimensional [17].

The conditions at which 3D MHD turbulence becomes quasi-two-dimensional and the formation of three dimensionality in Q2D turbulence have been clarified [10,13,18,19]. However, a clear path to Q2D turbulence from a quasi-two-dimensional laminar state is yet to be established. This question is specifically important in the context of duct flows and particularly in fusion blanket design. Indeed, if quasi-two-dimensional turbulence is to arise in blankets, it is unlikely to do so out of three-dimensional turbulence [1].

Research on transition to turbulence in MHD conduits has been mostly experimental [20] or based on fully three-dimensional simulations at moderate values of Ha (<100) and N, when the turbulent state can be expected to remain three dimensional [21,22]. However, these regimes stand very far from fusion relevant regimes (Ha $\simeq 10^4$). The only study to date approaching these regimes indicated that the growth of three-dimensional perturbations in electrically insulating ducts was impeded at Hartmann numbers as low as Ha $\simeq 300$, where the less efficient, quasi-two-dimensional Orr mechanism remains the only source of transient growth [23]. The corresponding optimal growth stood at least one order of magnitude below its 3D counterpart, raising the question as to whether the sort of subcritical transition normally associated with shear flows may indeed take place in the quasi-two-dimensional limit.

With these limitations in mind, a number of shallow water models can be derived to represent MHD flows in a quasi-two-dimensional state [10,24–26] very much in the spirit of shallow water models in rotating flows [27]. Such models have proved to be accurate, sometimes surprisingly so, for a number of complex flows including simple straight ducts [17,23,28], vortex lattices [29–31], sheared turbulence [24,32], flows around obstacles [33–37], and convective flows [38], linearly and nonlinearly. The clear advantage of these models is their low computational cost, as full three-dimensional numerics are prohibitively expensive for large Re, Ha, and N. As such, they offer a unique chance to identify and obtain insight into laminar to turbulent transitions in duct flows in these regimes.

In these regimes, traditional subcritical routes to turbulence may be obstructed, which would be detrimental to the efficient extraction of heat in the blanket coolant ducts [1]. Hence, beyond the classical Shercliff profile of insulating ducts [39], it is legitimate to consider whether alternative profiles may more efficiently generate turbulence or be less prone to suppressing it. As modifications to the base flow appear to be a more promising direction for turbulence suppression than influencing turbulent fields directly [40], it is instead worth exploring whether it is more efficient to select an
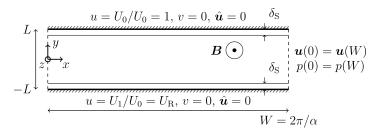
FIG. 1. Schematic diagram of the problem setup, with characteristic length of the duct half height L. The vertical dashed lines denote a periodicity constraint. The thick horizontal lines represent impermeable, no-slip boundaries, where the velocity is fixed (nondimensional boundary conditions provided), with an extent based on the streamwise wavelength or corresponding wave number being considered. Fully developed Shercliff boundary layers form on these walls, of thickness δ_S, which is a function of the friction parameter H. A uniform magnetic field is imposed normal to the page. The fixed out-of-plane Hartmann walls are the sources of the linear friction (not drawn).

optimal base flow, rather than an optimal perturbation, to generate and sustain turbulence. Although the flow was not natively quasi-two-dimensional, Refs. [40] and [41] applied forces designed to flatten the base flow away from the walls in an attempt to suppress turbulence. In both cases, the preferred force accelerates flow near the walls and decelerates flow in the bulk. Flatter base flows noticeably reduce turbulence production [42] and if sufficiently flattened can relaminarize the flow. This may take place in plug-like Shercliff flows. Linear transient growth was also found to be a good proxy for turbulent production far from the wall [42]. A different strategy was taken by Ref. [43], where base flow inflexion points were smoothed to eliminate turbulence. Conversely, Ref. [28] applied the inverse strategy of introducing inflexion points for the promotion of turbulence in MHD duct flows. As such, understanding the role of the base flow in the transition process appears to be crucial both in the fusion context and more generally. In particular, the questions we set out to answer are the following:

(1) What are the quasi-two-dimensional linear mechanisms promoting the growth of perturbations in quasi-two-dimensional duct flows?

(2) What is the nature of the bifurcation to any turbulent states that ensue?

(3) Can a subcritical transition take place at fusion-relevant parameters?

(4) Do the answers to these questions change, as the base flow profile is varied?

We address these questions by studying a quasi-two-dimensional wall-driven duct flow using the shallow water (SM82) model proposed in Ref. [10], where electromagnetic forces reduce to a linear friction exerted by the Hartmann layers on the bulk flow. The relative velocity of the walls can be continuously varied to achieve a range of base flows from symmetric to antisymmetric with an inflexion point. These flows are introduced in Sec. II. We then perform linear modal and nonmodal analyses to identify the linear growth mechanisms (Secs. III and V). A lower bound for their activation is obtained via the energy stability method (Sec. IV). The nature of the bifurcation is then sought through weakly nonlinear stability analysis (Sec. VI) before addressing the question of the fully nonlinear transition by means of two-dimensional DNS (Sec. VII) over a limited range of parameters.

II. PROBLEM FORMULATION

A. Problem setup

An incompressible Newtonian fluid, with density ρ, kinematic viscosity ν, and electrical conductivity σ flows through a duct of height $2L$ (y direction) and width a (z direction), see Fig. 1. The flow over a streamwise length W is periodic in the x direction. The duct walls are impermeable, no-slip,

and electrically insulating. Fluid motion is generated by the streamwise motion of the walls at $y = \pm L$, at dimensional velocities U_0 (top) and U_1 (bottom). A homogeneous magnetic flux density (hereafter magnetic field for brevity) $B\mathbf{e}_z$ pervades the entire domain. In the limit where the Lorentz force outweighs viscous and inertial forces, the flow is quasi-two-dimensional, with z variation of pressure and velocity exclusively localized in boundary layers on the out-of-plane walls. The bulk velocity outside these layers is $O(\mathrm{Ha})$ close to the local z-averaged velocity along the duct and accurately represented by the SM82 model [10],

$$\nabla_\perp \cdot \boldsymbol{u} = 0, \tag{1}$$

$$\frac{\partial \boldsymbol{u}}{\partial t} + (\boldsymbol{u} \cdot \nabla_\perp)\boldsymbol{u} = -\nabla_\perp p + \frac{1}{\mathrm{Re}}\nabla_\perp^2 \boldsymbol{u} - \frac{H}{\mathrm{Re}}\boldsymbol{u}, \tag{2}$$

where the last term on the right-hand side of Eq. (2) represents the source of friction. Here, the nondimensional variables t, p, and $\boldsymbol{u} = (u, v)$ represent time, pressure, and the 2D z-averaged velocity vector, respectively, while $\nabla_\perp = (\partial_x, \partial_y)$ and $\nabla_\perp^2 = \partial_x^2 + \partial_y^2$ are the 2D gradient and Laplacian operators, respectively. These were scaled by L/U_0, ρU_0^2, U_0, $1/L$, and $1/L^2$, respectively. The relevant nondimensional groupings are the Reynolds number (representing the ratio of inertial to viscous forces at the duct scale)

$$\mathrm{Re} = \frac{U_0 L}{\nu}, \tag{3}$$

and the friction parameter (representing the ratio of friction in the Hartmann layers to viscous forces at the duct scale)

$$H = 2\frac{L^2}{a^2}\mathrm{Ha} = 2\frac{L^2}{a^2}aB\left(\frac{\sigma}{\rho\nu}\right)^{1/2}. \tag{4}$$

The SM82 approximation assumes $\mathrm{Ha} \gg 1$ and $\mathrm{Ha}^2/\mathrm{Re} \gg 1$, which are obtainable for any H with appropriate choice of a, as discussed in Ref. [38]. The last governing nondimensional grouping is the dimensionless bottom wall velocity

$$U_\mathrm{R} = \frac{U_1}{U_0}. \tag{5}$$

U_R varies in the range $[-1, 1]$, where the quasi-two-dimensional counterpart of MHD-Couette flow is represented by $U_\mathrm{R} = -1$ and Shercliff flow by $U_\mathrm{R} = 1$.

B. Base flows

The steady, fully developed solution for the parallel base flow, $\boldsymbol{U} = U(y)\boldsymbol{e}_x$, without a driving pressure gradient, is

$$U(y) = C_1 \exp(-H^{1/2}y) + C_2 \exp(H^{1/2}y), \tag{6}$$

where

$$C_1 = \frac{U_\mathrm{R}\exp(H^{1/2}) - \exp(-H^{1/2})}{\exp(2H^{1/2}) - \exp(-2H^{1/2})}, \quad C_2 = \frac{\exp(H^{1/2}) - U_\mathrm{R}\exp(-H^{1/2})}{\exp(2H^{1/2}) - \exp(-2H^{1/2})}. \tag{7}$$

Example base flows for various values of U_R are provided in Fig. 2. $U_\mathrm{R} = -1$ constitutes the MHD-Couette limit, in which $U(y) = \sinh(H^{1/2}y)/\sinh(H^{1/2})$. This simplifies to pure Couette flow in the hydrodynamic case: As $H \to 0$, $U(y) = y$. $U_\mathrm{R} = 1$ constitutes the Shercliff limit, in which $U(y) = \cosh(H^{1/2}y)/\cosh(H^{1/2})$. This expression differs from the Shercliff profile derived by Ref. [17] for pressure-driven flows, by the finite wall velocity (an unavoidable translation), and by a negative multiplicative factor reflecting different ratios of centerline to bottom wall velocity in pressure-driven and wall-driven flows (the coefficient of Ref. [17] can be matched with appropriate choice of U_R, or by redefining Re). The Shercliff profile, with $U_\mathrm{R} = 1$, does not simplify to the Poiseuille
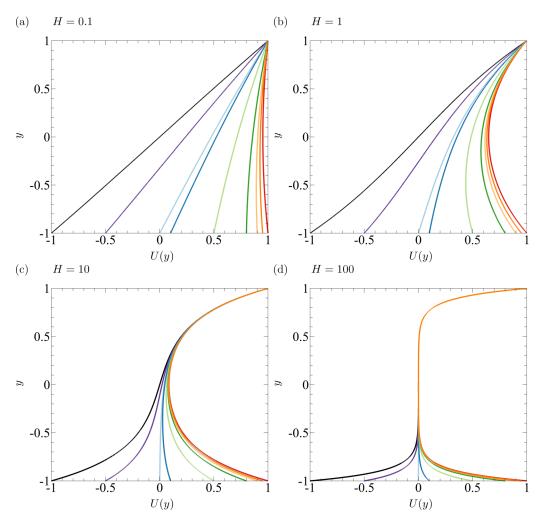
FIG. 2. Base flow profiles $U(y)$, at various H, for $U_R = -1, -0.5, 0, 0.1, 0.5, 0.8, 0.9, 0.95, 1$.

flow solution in the limit $H \to 0$ because of the absence of a pressure gradient, unlike the profile derived in Ref. [17]. In the hydrodynamic wall-driven flow, viscous diffusion is unopposed and the momentum imparted by the walls is fully diffused across the channel, unlike in finite pressure gradient Poiseuille flow. Interestingly, when $H > 0$ Hartmann friction balances diffusion in both wall- or pressure-driven flows, in an identical fashion, which explains the similarity between the profiles in this work and those in Ref. [17].

Varying U_R therefore varies the base flow through the family of MHD-Couette-Shercliff profiles. Unlike in the classical MHD-Couette or Shercliff flows, the nondimensional velocity $1 - U_{\min}$, where $U_{\min} = \min\{U(y)\}$, depends on the friction parameter H (recalling that velocities are nondimensionalized by U_0). Therefore, it is useful to express our results using an alternative definition of the Reynolds number

$$\mathrm{Re}_\Delta = \frac{U_\Delta L}{\nu} = \mathrm{Re}\,(1 - U_{\min}), \tag{8}$$

based on a velocity scale $U_\Delta = U_0\,(1 - U_{\min})$. Similarly, a nondimensional timescale $t_\Delta = t\,U_0/U_\Delta = t/(1 - U_{\min})$ is also defined.

C. Perturbation equations

Much of this work is dedicated to analyzing infinitesimal perturbations $(\hat{\boldsymbol{u}}, \hat{p})$ about the base flow,

$$\boldsymbol{u} = U(y)\mathbf{e}_x + \hat{\boldsymbol{u}}, \ p = \hat{p}. \tag{9}$$

The equations governing $\hat{\boldsymbol{u}}$ are obtained by substituting Eq. (9) into Eqs. (1) and (2) and neglecting terms of $O(|\hat{\boldsymbol{u}}|^2)$, yielding

$$\boldsymbol{\nabla}_\perp \cdot \hat{\boldsymbol{u}} = 0, \tag{10}$$

$$\frac{\partial \hat{\boldsymbol{u}}}{\partial t} + (\hat{\boldsymbol{u}} \cdot \boldsymbol{\nabla}_\perp)\boldsymbol{U} + (\boldsymbol{U} \cdot \boldsymbol{\nabla}_\perp)\hat{\boldsymbol{u}} = -\boldsymbol{\nabla}_\perp \hat{p} + \frac{1}{\mathrm{Re}}\nabla_\perp^2 \hat{\boldsymbol{u}} - \frac{H}{\mathrm{Re}}\hat{\boldsymbol{u}}. \tag{11}$$

On the lateral walls, $\hat{\boldsymbol{u}} = \partial_y\hat{\boldsymbol{u}} = 0$ boundary conditions are applied.

III. LINEAR STABILITY

A. Formulation

A sufficient condition for the base flow to be unstable is determined by seeking the least stable infinitesimal perturbation. Taking twice the curl of Eq. (11), substituting Eq. (10), and projecting along $\boldsymbol{e}_y$ provides an equation for the wall-normal component of the velocity perturbation

$$\frac{\partial}{\partial t}\nabla_\perp^2 \hat{v} = \frac{\partial^2 U}{\partial y^2}\frac{\partial}{\partial x}\hat{v} - U\frac{\partial}{\partial x}\nabla_\perp^2 \hat{v} + \frac{1}{\mathrm{Re}}\nabla_\perp^4 \hat{v} - \frac{H}{\mathrm{Re}}\nabla_\perp^2 \hat{v}. \tag{12}$$

As linearity is assumed, each mode evolves independently, with perturbations decomposed into plane waves (by virtue of the problem's invariance in the streamwise direction)

$$\hat{v}(y) = \mathrm{Re}\{\tilde{v}(y)e^{i\alpha x}e^{-i\lambda t}\}, \tag{13}$$

with eigenvalue λ, eigenvector $\tilde{v}(y)$, streamwise wave number α, exponential growth rate $\mathrm{Im}(\lambda)$, and wave speed $\mathrm{Re}(\lambda)/\alpha$. Substituting Eq. (13) into Eq. (12) provides an SM82 modification to the Orr-Sommerfeld equation [44],

$$[-i\lambda(D^2 - \alpha^2)]\tilde{v} = \left[i\alpha U'' - i\alpha U(D^2 - \alpha^2) + \frac{1}{\mathrm{Re}}(D^2 - \alpha^2)^2 - \frac{H}{\mathrm{Re}}(D^2 - \alpha^2)\right]\tilde{v}, \tag{14}$$

where, respectively, primes and D^n represent derivatives and the nth order derivative operator, with respect to y. Boundary conditions are now $\tilde{v} = D\tilde{v} = 0$.

Equation (14) is discretized with N_c Chebyshev collocation points [45]. Differentiation matrices $\boldsymbol{D^n}$ and boundary conditions are implemented following Ref. [46]. The eigenvalue problem is solved in MATLAB in the standard form at default tolerance of 10^{-14}. λ_j is defined as the jth eigenvalue of the discretized operator, sorted by descending growth rate, with corresponding eigenvector $\tilde{v}_j$. The critical Reynolds number is attained when $\mathrm{Im}(\lambda_1)$ is zero for a single wave number α_c. For the linear stability analysis, for all base flows, operators are discretized with $N_c = 200$, 350, 500, and 800 for $H \leqslant 10^2$, 5×10^2, 10^3, and 10^4, respectively, which ensures at least 30 Chebyshev points reside within a single Shercliff boundary layer. This enables the dominant wave number and growth rate to be determined to respective precisions of seven and nine significant figures (Table I). Spurious eigenvalues [47] are not an issue for the linear analysis, as they are situated sufficiently far below the real axis.

B. Results

The linear stability results for the family of Q2D mixed MHD-Couette-Shercliff flows are shown in Fig. 3. Figure 3(a) depicts the critical Reynolds number $\mathrm{Re}_{\Delta c}$ as a function of the friction parameter H. The symmetric Shercliff flow [17,38] has finite $\mathrm{Re}_{\Delta c}$ for all nonzero H. Once the

TABLE I. Resolution testing for eigenvalue problems. Left: energetic stability at $H = 100$, $\text{Re} = 500$, MHD-Couette flow ($U_R = -1$). Right: linear stability at $H = 1000$, $\text{Re} = 10^7$, Shercliff flow ($U_R = 1$). The bold resolutions were chosen, as discussed in Secs. III A and IV A. $\alpha_{\max}$ is the wave number with max $[\text{Im}(\lambda_1)]$ for a given Re.

N_c	$\alpha_{\max}$	$10^1 \max [\text{Im}(\lambda_1)]$	N_c	$\alpha_{\max}$	$10^2 \max [\text{Im}(\lambda_1)]$
20	6.38246470	-1.53187927830825	200	3.48248937	1.78999418074040
40	6.42263964	-1.53055895392212	300	3.47528224	1.79276681627594
60	6.42263962	-1.53055895418749	400	3.47527862	1.79275949928794
80	6.42263963	-1.53055895418486	**500**	3.47527864	1.79275949851556
100	6.42263954	-1.53055895418970	600	3.47527873	1.79275949846157

symmetry of the base flow is broken, a value of H, $H^\infty(U_R)$ exists, below which the critical Reynolds number is infinite. Hence, except for the symmetric Shercliff flow, $\text{Re}_{\Delta c}$ can initially be reduced with increasing H. $\text{Re}_{\Delta c}$ decreases to a minimum for $H > H^\infty$, so that past this minimum, increasing the friction parameter stabilizes all flows to infinitesimal perturbations ($\text{Re}_{\Delta c}$ increases monotonically with increasing H). A greater degree of antisymmetry (U_R closer to -1) requires a larger value of H before the critical Reynolds number becomes finite (H^∞ monotonically increases with decreasing U_R), and provides increasing stability to infinitesimal perturbations. As such, the antisymmetric MHD-Couette flow is the most stable base flow for a given H and has finite $\text{Re}_{\Delta c}$ for $H \gtrsim 15.102$. The asymptotic behavior is also reflected in the critical wave numbers, Fig. 3(b), where $\alpha_c \to 0$ for sufficiently small H. As discussed in Ref. [48], disturbances with finite wavelength are stable in the inviscid limit, $\text{Re}_\Delta \to \infty$. Hence, a finite wave number cannot be maintained as $\text{Re}_{\Delta c} \to \infty$.

As observed in Ref. [49] for the even and odd modes of Hartmann flow, the asymptotic behavior ($\text{Re}_{\Delta c} \to \infty$, $\alpha_c \to 0$) is explained by the interaction between the Tollmien-Schlichting (TS) wave
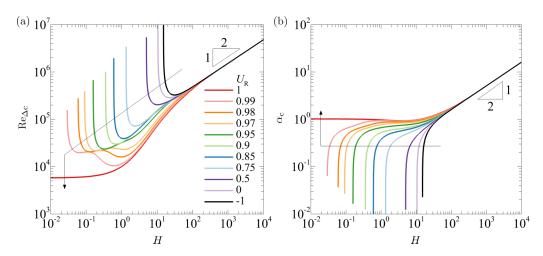

FIG. 3. Linear stability results, with arrows indicating increasing U_R. (a) Critical Reynolds number. (b) Critical wave number. $\text{Re}_c \to \infty$ asymptotes are computed to $\text{Re} = 10^7$. As $H \to \infty$, $\text{Re}_{\Delta c} = 4.83468 \times 10^4 \, H^{1/2}$ and $\alpha_c = 0.161513 H^{1/2}$, which agree well with Ref. [17]. As $H \to 0$, $\text{Re}_{\Delta c} \to 5772.22$ for $U_R = 1$. MHD-Couette ($U_R = -1$) results are modified by a factor of $1/2$. The isolated boundary layer on the top wall sees an effective local minimum velocity of $U_{\min,\text{eff}} = 0$, just at the edge of the boundary layer. However, the velocity profile across the entire duct still has $U_{\min} = -1$, at the bottom wall, resulting in $(1 - U_{\min,\text{eff}})/(1 - U_{\min}) = 1/2$.
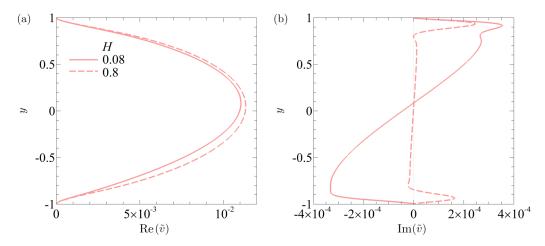
FIG. 4. Eigenvectors $\tilde{v}_1$ from the linear stability analysis, $U_R = 0.99$ ($H^\infty = 0.02898$). Comparison between $H = 0.8$, $\mathrm{Re}_{\Delta c} = 1.07724 \times 10^4$ ($\mathrm{Re}_{\Delta c}$ is smaller, due to constructive interference; indicated by approximate symmetry in imaginary component) and $H = 0.08$, $\mathrm{Re}_{\Delta c} = 1.99932 \times 10^4$ ($\mathrm{Re}_{\Delta c}$ is larger, due to destructive interference; indicated by approximate antisymmetry in imaginary component). (a) Real components. (b) Imaginary components.

structures running along the top and bottom walls. Note that as the base flow is not symmetric (respectively, antisymmetric) unless $U_R = 1$ (respectively, $U_R = -1$), the entire domain $y \in [-1, 1]$ is always simulated. This allows natural, sometimes approximate, symmetries in the dominant eigenmode to be observed. For symmetric modes, which can only be supported by symmetric base flows, the instabilities at the top and bottom walls rotate in the same direction, and constructively interfere along the centerline, causing additional destabilization (compared to an isolated TS wave). For antisymmetric modes, the instabilities rotate in the opposite direction along the top and bottom walls, and hence destructively interfere. The destructive interference is maximum at $U_R = -1$ and $H = 0$, to the point of preventing the growth of any perturbation, such that $\mathrm{Re}_{\Delta c}$ diverges in this limit. Increasing H from 0, for a given value of U_R, reduces the length scale of the TS waves attached to the top and bottom wall, causing them to separate from each other, which reduces interference. For $H > H^\infty$, the destructive interference between TS waves is insufficient to prevent the growth of all perturbations and the flow becomes linearly unstable. Subsequent increases in H further reduce the level of destructive interference, leading to a drop in $\mathrm{Re}_{\Delta c}(H)$. Once all destructive interference has been eradicated, a subsequent increase in H only results in higher friction that impedes modal growth. As such, $\mathrm{Re}_{\Delta c}(H)$ increases. This explains the presence of a minimum in $\mathrm{Re}_{\Delta c}(H)$. Similarly, increasing U_R progressively from -1 introduces increasingly more symmetry in the most unstable mode, which forms an alternate means of decreasing the amount of destructive interference. As such, lower values of H become sufficient to suppress complete destructive interference, and $H^\infty(U_R)$ decreases monotonically with increasing U_R. For U_R sufficiently close to 1, and for H sufficiently above H^∞, the mode can even experience noticeable constructive interference (resulting in a second set of local minima, recalling Fig. 3, which appear slightly above the curve for the purely symmetric $U_R = 1$ case). A comparison of the two local minima is considered in Fig. 4, for $U_R = 0.99$ (almost symmetric base flow). The degree of symmetry in the imaginary component of the eigenvector provides a clear indication of the type of interference. There is a much greater degree of antisymmetry in the imaginary component at $H = 0.08$, near the first local minimum, indicating some destructive interference, than at $H = 0.8$, near the second local minimum, which experiences significant constructive interference (the imaginary component is almost symmetric). However, as the real component has a much larger magnitude than the imaginary component, the overall mode structures look very similar.
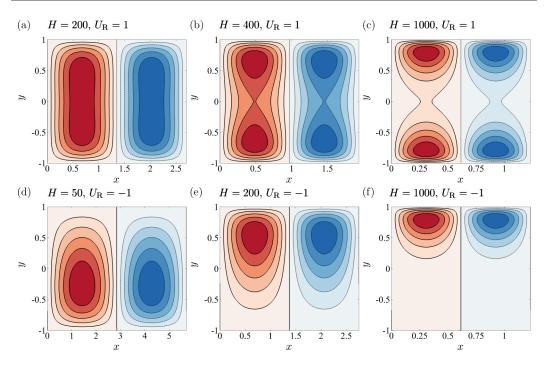
FIG. 5. Dominant eigenvectors of the linear stability analysis, $\hat{v}$-velocity contours; solid lines (red flooding) positive; dotted lines (blue flooding) negative. [(a)–(c)] Shercliff flow. [(d)–(f)] MHD-Couette flow.

The collapse of the critical Reynolds numbers and wave numbers in the limit $H \to \infty$ is due to the isolation of the boundary layers, already noted for Shercliff [17] and Hartmann layers [50,51]. For these large H, the critical Reynolds numbers and wave numbers scale with $H^{1/2}$, consistent with the thickness of a Shercliff boundary layer. The separation mechanism for TS waves at high H is illustrated in Fig. 5, for Shercliff [Figs. 5(a)–5(c)] and MHD-Couette [Figs. 5(d)–5(f)] flows. The TS wave pattern in the Shercliff flow displays the progressive separation of one central wave structure into two distinct TS wave structures as H increases, as found in the Hartmann flow [52]. Conversely, for flows with any degree of antisymmetry (excepting MHD-Couette flow) the velocity gradient at one wall will always be larger than at the other, drawing and confining the central mode toward the more highly sheared wall region as H increases, which isolates the modes to a greater degree when U_R is smaller, for a given H.

IV. ENERGETIC ANALYSIS

A. Formulation

The largest Reynolds number at which any perturbation would decay monotonically, Re_E, is determined from the equation governing the evolution of the perturbation energy. Following Ref. [44], taking the dot product of the perturbation u_i with Eq. (11) and integrating over a volume V, such that all divergence terms vanish, yields

$$\frac{dE}{dt} = -\frac{1}{2} \int_V u_i u_j \left(\frac{\partial U_i}{\partial x_j} + \frac{\partial U_j}{\partial x_i} \right) dV - \frac{1}{Re} \int_V \frac{\partial u_i}{\partial x_j} \frac{\partial u_i}{\partial x_j} dV - 2E \frac{H}{Re}. \tag{15}$$

The terms on the right-hand side respectively describe energy transfer from mean shear, viscous dissipation, and Hartmann friction [17]. The perturbation that maximizes 1/Re is found by using variational calculus and introducing a Lagrange multiplier to enforce the constraint of mass
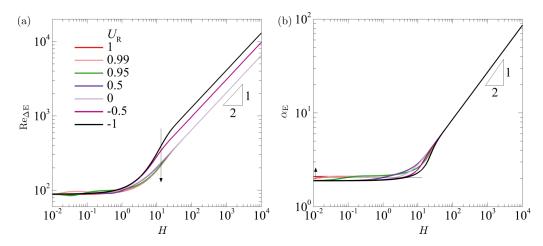
FIG. 6. Energetic analysis results, with arrows indicating increasing U_R. (a) Energy Reynolds number ($U_R = -1$ and -0.5 cases collapse at high H if Re_E is plotted, but appear translated with $Re_{\Delta E}$ plotted, as discussed for $U_R = -1$ in the caption of Fig. 3). (b) Energy wave number. As $H \to \infty$, $Re_{\Delta E} = 65.3288H^{1/2}$ and $\alpha_E = 0.863470H^{1/2}$, which agree well with Ref. [17]. As $H \to 0$, $Re_{\Delta E} \to 87.5933$ for $U_R = 1$.

conservation [44,53,54], which, once eliminated and when we seek plane-wave solutions, leads to the following eigenvalue problem:

$$[-i\lambda_E(D^2 - \alpha^2)]\tilde{v}_E = \left[\frac{1}{2}i\alpha U'' + i\alpha U'D + \frac{1}{Re}(D^2 - \alpha^2)^2 - \frac{H}{Re}(D^2 - \alpha^2)\right]\tilde{v}_E. \qquad (16)$$

Equation (16) is discretized and solved in an identical manner to the linear stability problem in Sec. III A. Re_E is obtained when the largest imaginary component over all eigenvalues $\lambda_{E,j}$ is zero for a single wave number α_E. $N_c = 60$, 80, and 140 for $H \leqslant 10^2$, 10^3, and 10^4 again allow the dominant wave number and growth rate to be determined to respective precisions of seven and nine significant figures (Table I).

B. Results

The energetic Reynolds numbers are shown in Fig. 6(a). Unlike the linear stability analysis, Fig. 3(a), none of the curves asymptote to infinite Reynolds number, for profiles with any degree of antisymmetry, at low H. Overall, the energetic analysis indicates a limited influence of the base flow profile, as using the appropriate velocity scale in the Reynolds number, the results are virtually coincident for all MHD-Couette-Shercliff profiles, for all H. Note that in the high-H region, the curves collapse in Re_E rather than $Re_{\Delta E}$, as only the local difference in the maximum and minimum velocity over an isolated boundary layer is important. The collapse to dynamics dominated by an isolated boundary layer occurs for all base flows simultaneously, and is initiated at much lower H ($H \gtrsim 30$) than the linear analysis (which collapses between $H \gtrsim 300$ for $U_R = -1$ to $H \gtrsim 1000$ for $U_R = 1$). The wave numbers from the energetic analysis, Fig. 6(b), are also notably larger than those from the linear stability analysis, Fig. 3(b).

The eigenvectors from the energetic analysis are provided in Fig. 7. Unlike the linear stability analysis, these modes do not directly represent solutions to the SM82 equations [17]. Similar to the linear stability analysis, at higher H, a wall mode forms, which again is increasingly compacted toward the wall as H increases. Discounting the irrelevant symmetry or antisymmetry, as in focusing on $-1 < y < 0$ in Fig. 7, the modes effectively appear identical. Thus, varying the base flow through
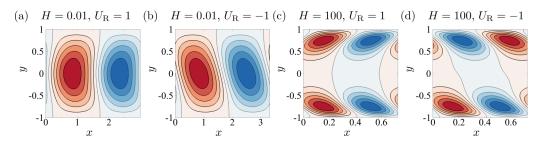
FIG. 7. Dominant eigenvectors of the energetic analysis, comparing Shercliff and MHD-Couette flows, $\hat{v}$-velocity contours: solid lines (red flooding) are positive; dotted lines (blue flooding) are negative.

U_R has little effect on the overall dynamics of the dominant modes of the energetic analysis (when comparing the same H).

V. LINEAR TRANSIENT GROWTH AND PSEUDOSPECTRA

A. Formulation

A lower bound for the Reynolds number at which an instability exponentially grows, and an upper bound on the Reynolds number at which all instabilities monotonically decay, have been derived in the preceding sections. However, nonorthogonality of the linearized evolution operator can lead to the transient growth of a superposition of linearly decaying eigenvectors [44]. To this end, transient growth analysis is performed for $\mathrm{Re_E} < \mathrm{Re} \lesssim \mathrm{Re_c}$. The maximum possible transient growth is found by seeking the initial condition for perturbation $\hat{\mathbf{u}}_\tau(t=0)$ that maximizes the gain functional $G = ||\hat{\mathbf{u}}(t=\tau)||/||\hat{\mathbf{u}}(t=0)||$ at prescribed time $t=\tau$ of the pertubation's linearized evolution. G represents the gain in perturbation kinetic energy as per Ref. [55] under the norm $||\hat{\boldsymbol{u}}|| = \int \hat{\boldsymbol{u}} \cdot \hat{\boldsymbol{u}} \, d\Omega$, where Ω represents the computational domain. The maximum possible gain $G_{\max}$ is found at optimal time τ_{opt} for which the value $G_{\max}(\tau_{\mathrm{opt}})$ of the optimized functional is maximum. In practice, since $\hat{\mathbf{u}}$ is a plane wave, $\hat{v}_\tau(t=0)$ is obtained as the solution of an optimization problem with the linearized evolution equation

$$\frac{\partial \hat{v}}{\partial t} = (D^2 - \alpha^2)^{-1} \left[-i\alpha U(D^2 - \alpha^2) + i\alpha U'' + \frac{1}{\mathrm{Re}}(D^2 - \alpha^2)^2 - \frac{H}{\mathrm{Re}}(D^2 - \alpha^2) \right] \hat{v} \qquad (17)$$

as constraint. The optimal is obtained iteratively from a timestepper, set up in MATLAB, which first evolves Eq. (17) to time τ, then evolves the adjoint equation

$$\frac{\partial \hat{\xi}}{\partial t} = (D^2 - \alpha^2)^{-1} \left[i\alpha U(D^2 - \alpha^2) + 2i\alpha U'D + \frac{1}{\mathrm{Re}}(D^2 - \alpha^2)^2 - \frac{H}{\mathrm{Re}}(D^2 - \alpha^2) \right] \hat{\xi}, \qquad (18)$$

for the Lagrange multiplier of the velocity perturbation $\hat{\xi}$, from $t=\tau$ to $t=0$, until $\hat{\mathbf{u}}_\tau(t=0)$ has converged to the desired precision. A third-order forward Adams-Bashforth scheme [56] is used to integrate Eqs. (17) and (18) in time, subject to $\hat{v}$ and $\hat{\xi}$ satisfying boundary conditions $\hat{v} = D\hat{v} = \hat{\xi} = D\hat{\xi} = 0$ at all walls, and "initial" condition $\hat{\xi}(\tau) = \hat{v}(\tau)$. The jth eigenvalue $\lambda_{G,j}$ of the operator representing the action of direct then adjoint evolution is determined with a Krylov subspace scheme [55,57]. With eigenvalues sorted in descending order by largest real component, the optimized growth $G = \lambda_{G,1}$. The iterative scheme is initialized with random noise for $\hat{v}(t=0)$.

Validation against literature is provided in Table II. Validation against the rescaled results of Ref. [58] is also visible in Fig. 8. To maintain six significant figure accuracy in $G_{\max}$ requires a time step of $\Delta t = 2 \times 10^{-5}$, 20 forward-backward iterations, and $N_c = 60$, 80 and 100 Chebyshev points for $H \leqslant 10$, 30, and 100, respectively (for $\mathrm{Re} \leqslant 10^5$). τ_{opt} and α_{opt} are computed to three significant figures.

TABLE II. Comparisons of the G_{max} calculated in the present work, and those calculated by Ref. [23] for various H, MHD-Poiseuille flow profile, at Re $= 5 \times 10^3$ and 1.5×10^4. The results of Ref. [23], kindly provided from their Fig. 2, are wave number optimized in a full three-dimensional domain, but time optimized at the 3D optimal wave number in a two-dimensional domain. The discrepancy at low H reflects the breakdown of the quasi-two-dimensionality assumption, not numerical error.

	Re $= 5 \times 10^3$			Re $= 1.5 \times 10^4$		
H	Ref. [23]	Present	Error (%)	Ref. [23]	Present	Error (%)
10	14.65	14.8272	1.195	27.4	34.0552	19.542
30		7.62330		17.7	17.7515	0.290
50	6.08	6.13073	0.827	14.2	14.4036	1.414
100	4.61	4.60979	0.004	11.0	11.0476	0.431
150	3.88	3.89381	0.355	9.43	9.44834	0.194
300	2.90	2.90575	0.198	7.11	7.19654	1.203
600	2.16	2.16392	0.181	5.43	5.44425	0.262
800	1.91	1.91680	0.355	4.83	4.83895	0.185

Additionally there was excellent agreement with results obtained with the matrix method (provided in Appendix A of Ref. [44]) at low Reynolds and Hartmann numbers. As such, the matrix method is used to further assess the transient growth capability by considering the non-normality of the operator, via the pseudospectrum and condition number of the energy norm weight matrix. A point z on the complex plane is within the ϵ_p pseudospectrum of the SM82-modified Orr-Sommerfeld operator if $||(zI - \mathcal{L}_{OS})^{-1}|| \geqslant \epsilon_p^{-1}$ [59]. For a normal operator, a point z on the complex plane will be at most at a distance ϵ_p from any eigenvalue. A greater degree of non-normality is correlated with a greater ratio of the distance between a point z and the nearest eigenvalue, to the bounding value of ϵ_p at the point z. The extent of the pseudospectra into the complex upper half-plane forms a lower bound on transient growth [44,46,59–61]. The pseudospectrum is computed by evaluating $||W (1/(zI - \lambda))W^{-1}||_2$, with energy norm weight matrix W [44], identity matrix I, and diagonalized eigenvalues λ of the discretized SM82-modified Orr-Sommerfeld operator. Computations were performed with a discretization of $N_c = 400$ and truncated to the 240 modes with largest imaginary component.

B. Results: Transient growth

The optimized growth for various base flows, over a range of H values, is depicted in Fig. 8. Unlike in 3D flows where the lift-up mechanism incites significant growth [44,62], Q2D transient growth is driven by the less efficient Orr mechanism. The maximum transient growth found in the present study is accordingly lower, scaling as $G_{max} \sim \mathrm{Re}^{2/3}$, with magnitudes of only $G_{max} \simeq 10^2$ for Reynolds numbers of 10^4 to 10^5, depending on H and U_R. At $H = 30$, the transient growth already closely matches that of an isolated exponential boundary layer (long dashed lines in Fig. 8) for all U_R. By $H = 100$, G_{max}, α_{opt}, and τ_{opt} all respectively collapse to that limit. As in the energetic analysis, this collapse occurs at far lower H than the linear stability analysis. This could be due to the much larger wave numbers at which the transient growth and energetic analysis optimals occur. The TS waves thereby penetrate a shorter distance into the bulk (see Fig. 9) and therefore become isolated at a smaller friction parameter. The TS wave optimals otherwise have the same general appearance as the linear stability eigenmodes (Fig. 5), except that both MHD-Couette and Shercliff flows have wave structures at both walls, which thereby require similar friction parameters to isolate. This leads to the overall difference in transient growth across the family of profiles to be negligible even at relatively low $H \geqslant 30$. Constructive interference between modes at the top and bottom walls may be the cause of the slightly larger growth observed for symmetric base flows at smaller
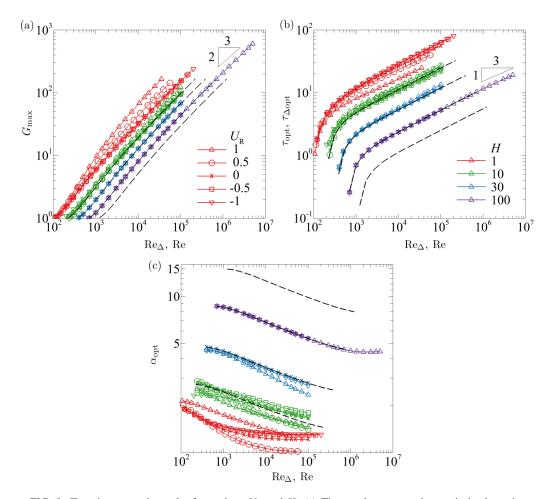
FIG. 8. Transient growth results for various U_R and H. (a) Time and wave number optimized maximum growth. (b) Optimal time interval. (c) Optimal wave number. Re_Δ and $\tau_{\Delta\mathrm{opt}} = \tau_{\mathrm{opt}}/(1 - U_{\min})$ are plotted for $H = 1$, and Re and τ_{opt} for $H = 10, 30$, and 100. The black long dashed lines correspond to an isolated Shercliff boundary layer [58], at $H = 10, 30, 100$, and 300. For these, plotted quantities are $\mathrm{Re} = \mathrm{Re}_S\, H^{1/2}$, $\alpha_{\mathrm{opt}} = \alpha_{\mathrm{opt},S}\, H^{1/2}$, and $\tau_{\mathrm{opt}} = \tau_{\mathrm{opt},S}/H^{1/2}$. The $\mathrm{Re}^{2/3}$ and $\mathrm{Re}^{1/3}$ power laws for $G_{\max}$ and τ_{opt} are approximate.

H. However, even this is not large, such that the base flow does not make a significant difference in generating Q2D linear transient growth. Furthermore, the degree of symmetry in the base flow is not relevant once H is sufficiently large to flatten the central region, and isolate the boundary layers, after which all growth values collapse to those of an isolated exponential boundary layer.

C. Results: Pseudospectra

The transient growth results are also supported by the pseudospectra. Figure 10 depicts pseudospectra obtained at $\mathrm{Re}_\Delta \approx 10^4$ for both the Shercliff and MHD-Couette base flows, at $H = 10$ and $H = 100$. Increasing the Reynolds number directly brings more eigenvalues close to the real axis, allowing smaller perturbations to cross to the positive imaginary half-plane, thereby generating more transient growth [59]. However, as demonstrated in Fig. 10, increasing the Hartmann friction parameter mainly stretches the pseudospectra along the real axis, with the further separation of the eigenvalues appearing to lead to reduced transient growth for a given Reynolds number. This is
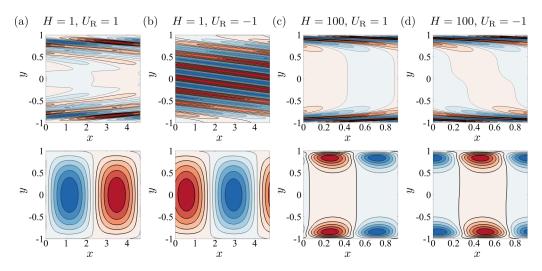
FIG. 9. Optimized perturbations at $\mathrm{Re}_\Delta \approx 10^4$, at $t = 0$ (top row) and linearly evolved to $t = \tau_{\mathrm{opt}}$ (bottom row), comparing Shercliff and MHD-Couette flows. $\hat{v}$-velocity contours: solid lines (red flooding) are positive; dotted lines (blue flooding) are negative.

supported by determining the condition number of the basis, $\kappa = ||\boldsymbol{W}||_2 ||\boldsymbol{W}^{-1}||_2$ [44,59], recalling that a normal operator has a condition number of unity. At or near hydrodynamic conditions, the condition number of MHD-Couette flow is much higher than for Shercliff flow. This was observed in 3D non-MHD Couette and Poiseuille flows [59] and remains unexplained. For example, at $H = 1$, $\mathrm{Re}_\Delta \approx 10^3$, the condition numbers for Shercliff and MHD-Couette flows are 1.9×10^3 and 1.2×10^8, respectively (at α_{opt}). However, at $H = 100$, $\mathrm{Re}_\Delta \approx 10^3$, the condition numbers are respectively 1.0×10^4 and 1.3×10^6. Hence, an increasing Hartmann friction parameter acts to reorient eigenvectors such that they are more normal for MHD-Couette flow and less normal for Shercliff flow. It also indicates the increasing similarity between these base flow profiles with increasing H.

VI. WEAKLY NONLINEAR STABILITY

A. Formulation

By assuming a small perturbation amplitude $\mathcal{O}(\epsilon)$, to allow linearization, linear stability analysis becomes amplitude independent. However, if amplitude dependence is maintained, a weakly nonlinear analysis can be performed. To remain accurate, the weakly nonlinear analysis is concerned only with expansion about a leading perturbation which is close to neutrally stable. This ensures only one mode is unstable [53]. Linearly, a single unstable mode would either slowly grow or decay exponentially. However, if weakly nonlinear self-interaction occurs, the overall growth rate will increase or decrease, depending on whether the leading nonlinear growth term is positive or negative. A positive nonlinear growth can outweigh a negative linear growth rate if the linear growth is sufficiently small (close to the neutral curve), such that growth occurs at $\mathrm{Re} < \mathrm{Re_c}$ until a saturation amplitude, or a turbulent state, is reached (in which case the bifurcation is subcritical). If the nonlinear term is negative, $\mathrm{Re} > \mathrm{Re_c}$ is required for nontransient growth (the bifurcation is supercritical). The amplitude dependence of the plane-wave mode $\hat{w}_n(y) = w(y)e^{i\alpha n x}$ is expanded as

$$\hat{w}_n = \sum_{m=0}^{\infty} \epsilon^{|n|+2m} \tilde{A}^{|n|} |\tilde{A}|^{2m} \hat{w}_{n,|n|+2m}, \tag{19}$$

where $\hat{w}_{n,|n|+2m}$ now denotes a perturbation (the first subscript is the harmonic, the second is the amplitude), in line with Ref. [49], and $\tilde{A} = A/\epsilon$ is the normalized amplitude. The wave frequency
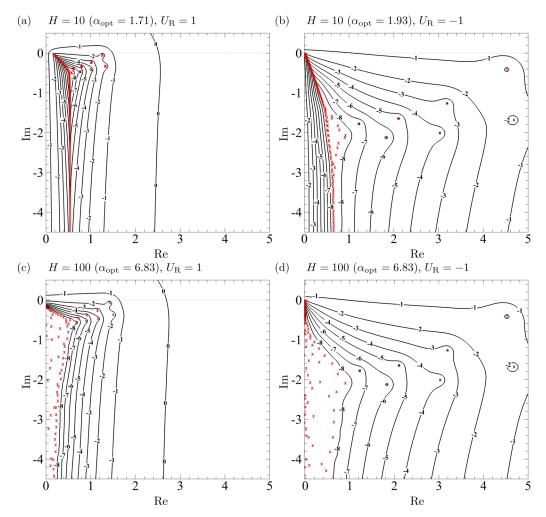
(a) $H = 10$ ($\alpha_{\mathrm{opt}} = 1.71$), $U_R = 1$

(b) $H = 10$ ($\alpha_{\mathrm{opt}} = 1.93$), $U_R = -1$

(c) $H = 100$ ($\alpha_{\mathrm{opt}} = 6.83$), $U_R = 1$

(d) $H = 100$ ($\alpha_{\mathrm{opt}} = 6.83$), $U_R = -1$

FIG. 10. Pseudospectra (contours from 10^{-8} to 1, labeled by exponent) at $\mathrm{Re}_\Delta \approx 10^4$, comparing Shercliff and MHD-Couette flows (the latter symmetric about the imaginary axis). Red crosses denote eigenvalues from the linear stability analysis λ, computed at the same parameters as the linear transient optima.

ω is also expanded as $\omega = \omega_0 + \epsilon^2 \tilde{\omega}_2 + \cdots$, where the normalized amplitude $\tilde{\omega}_2 = \omega_2/\epsilon^2$. The linearly unstable mode $\hat{w}_{1,1}$ (which is $\hat{v}$ under rescaling) of $\mathcal{O}(\epsilon)$ excites via self-interaction through the nonlinear term a second harmonic $\hat{w}_{2,2}$ and a modification to the base flow $\hat{u}_{0,2}$ (zeroth harmonic), which both have amplitude of $\mathcal{O}(\epsilon^2)$ [49]. These harmonics also interact with the original perturbation, resulting in another harmonic $\hat{h}^w_{1,3}$ with amplitude of $\mathcal{O}(\epsilon^3)$ [49]. Higher order terms are neglected, as they have a rapidly increasing radius of convergence [44]. However, such an expansion is sufficient to define the bifurcation type as sub- or supercritical and determine whether the system is sensitive to subcritical perturbations of finite amplitude.

The weakly nonlinear stability is calculated following the method outlined in Ref. [49], where the key equations are provided here. Denoting $U = \hat{u}_0$ in line with Ref. [49], the equations governing higher order harmonics of the base flow and the perturbation are

$$D^2 \hat{u}_{0,2m} - H \hat{u}_{0,2m} = \hat{g}_{0,2m}, \tag{20}$$

$$\mathcal{L}_n \hat{w}_n = \left[(D_n^2 - i\lambda n) D_n^2 - H D_n^2 - i\alpha n (\hat{u}_0'' - u_{0,0} D_n^2) \right] \hat{w}_n = \hat{h}^w_{n,|n|+2m}, \tag{21}$$

respectively, where $D_n = \partial/\partial y \boldsymbol{e}_y + in\alpha \boldsymbol{e}_x$ and where the right-hand sides, representing the curl of the nonlinear term, are

$$\hat{g}_{0,2m} = i \sum_{m \neq 0}^{\infty} (\alpha m)^{-1} \hat{w}_m^* D^2 \hat{w}_m, \tag{22}$$

$$\hat{h}_{n,|n|+2m}^w = n \sum_{m \neq 0}^{\infty} m^{-1} \big(\hat{w}_{n-m} D_m^2 D \hat{w}_m - D(\hat{w}_m) D_{n-m}^2 \hat{w}_{n-m} \big). \tag{23}$$

Here $*$ denotes complex conjugation. Equations (20) and (21) are identical to those used to determine the base flows in Sec. II B and the linear stability results in Sec. III, respectively, if the right-hand sides are set to zero (taking $m = 0$, $n = 1$). Equations (20) through (23) are discretized into matrix operators and solved as follows, noting that after determining the right-hand sides of Eqs. (20) and (21), the amplitude expansion for $\hat{w}_n$ should be substituted in. First, the SM82-modified Orr-Sommerfeld eigenvalue problem

$$\big[\boldsymbol{A}_1^{-1} \boldsymbol{M}_1(u_{0,0}) - \lambda \boldsymbol{I} \big] w_1 = 0 \tag{24}$$

is solved in the standard form, which provides the leading eigenvalue λ_1, with frequency $\omega_0 = \mathrm{Im}(\lambda_1)$, and the corresponding right and left eigenvectors, $w_{1,1}$ and $w_{1,1}^\dagger$, respectively. Re_c and α_c are determined from the linear stability problem, Eq. (24), with neutral conditions satisfying $\mathrm{Re}(\lambda_1) = 0$ in this formulation. The following are then solved:

$$u_{0,2} = -2\alpha^{-1} (\boldsymbol{D}^2 - H\boldsymbol{I})^{-1} \mathrm{Im}(w_{1,1}^* \boldsymbol{F}_0 \boldsymbol{D}^2 w_{1,1}), \tag{25}$$

$$w_{2,2} = (\boldsymbol{M}_2 - 2i\omega_0 \boldsymbol{A}_2)^{-1} [2\boldsymbol{F}_2 \boldsymbol{D}(\boldsymbol{D}(w_{1,1} \boldsymbol{D} w_{1,1}) - 2(\boldsymbol{D} w_{1,1})^2)], \tag{26}$$

$$h_{1,3}^w = 0.5[w_{1,1}^* \boldsymbol{A}_2 \boldsymbol{D} w_{2,2} - \boldsymbol{D}(w_{2,2}) \boldsymbol{A}_1 w_{1,1}^*] - [w_{2,2} \boldsymbol{A}_1 \boldsymbol{D} w_{1,1}^* - \boldsymbol{D}(w_{1,1}^*) \boldsymbol{A}_2 w_{2,2}], \tag{27}$$

where

$$\boldsymbol{A}_n = \boldsymbol{D}^2 - n^2 \alpha^2 \boldsymbol{I}, \quad \boldsymbol{N}_n(u_{0,0}) = i\alpha(u_{0,0}'' \boldsymbol{I} - u_{0,0} \boldsymbol{A}_n), \quad \boldsymbol{M}_n = \boldsymbol{F}_n \big[\boldsymbol{A}_n^2 - H\boldsymbol{A}_n + \mathrm{Re} \boldsymbol{N}_n \big], \tag{28}$$

with boundary condition matrix $\boldsymbol{F}_n$ as given in Refs. [47,49]. $w_{1,1}$ is normalized such that $\boldsymbol{D}^2 w_{1,1}(1) = 1$, and $w_{1,1}^\dagger$ such that $w_{1,1} \cdot w_{1,1}^\dagger = 1$.

The $n = 3$ harmonic of Eq. (21) only has a solution when the right-hand side is not proportional to $w_{1,1}$. Thus, the right-hand side must be orthogonal to the adjoint eigenfunction $w_{1,1}^\dagger$ [49]. The $n = 3$ harmonic is

$$\big(\boldsymbol{A}_1^{-1} \boldsymbol{M}_1 - i\omega_0 \boldsymbol{I} \big) w_{1,3} = \boldsymbol{A}_1^{-1} \big(\boldsymbol{F}_1 h_{1,3}^w + |A|^{-2} \{ \boldsymbol{F}_1 \boldsymbol{N}_1 [(\mathrm{Re} - \mathrm{Re}_c) u_0 + |A|^2 u_{0,2}] + i\omega_2 \boldsymbol{A}_1 \} w_{1,1} \big). \tag{29}$$

The right-hand side will be zero once orthogonal to $w_{1,1}^\dagger$ if the frequency perturbation satisfies

$$i\omega_2 = \mu_1 (\mathrm{Re} - \mathrm{Re}_c) + \mu_2 |A|^2, \tag{30}$$

where

$$\mu_1 = w_{1,1}^\dagger \cdot \boldsymbol{A}_1^{-1} \boldsymbol{F}_1 \boldsymbol{N}_1 w_{1,1}, \tag{31}$$

$$\mu_2 = w_{1,1}^\dagger \cdot \boldsymbol{A}_1^{-1} \boldsymbol{F}_1 \big(\boldsymbol{N}_1(u_{0,2}) w_{1,1} - h_{1,3}^w \big). \tag{32}$$

The linear growth rate correction is then $\mu_1 (\mathrm{Re} - \mathrm{Re}_c)$ and the first Landau coefficient μ_2 [44,53]. Rearranging the real part of Eq. (30) yields $|A|^2 = -(\mathrm{Re} - \mathrm{Re}_c) \mathrm{Re}(\mu_1)/\mathrm{Re}(\mu_2)$. Thus, $\mathrm{Re}(\mu_1) > 0$ is required for the existence of a finite amplitude state, while $\mathrm{Re}(\mu_2) > 0$ (respectively, $\mathrm{Re}(\mu_2) < 0$) defines a subcritical (respectively, supercritical) bifurcation. Note that all coefficients quoted in this paper are rescaled by $\alpha^2 \mathrm{Re}$, following Refs. [49] and [63].

Weakly nonlinear analysis is valid only near the neutral curve, such that only one mode is ever unstable. However, MHD-Couette flow yields a conjugate pair of equally unstable modes.

TABLE III. Resolution testing for the weakly nonlinear analysis, MHD-Couette flow ($U_R = -1 + 10^{-10}$) at $H = 1000$, $\mathrm{Re_c} = 1.52886\times10^6$, $\alpha_c = 5.10748$. The bold resolution was chosen, identical to that for the linear stability analysis.

N_c	10^{-6} Re (μ_1)	10^{-8} Im (μ_1)	10^3 Re (μ_2)	10^4 Im (μ_2)
400	1.02741326199010	−1.78689676323013	1.08671495177896	5.88065081880331
500	1.02741326027113	−1.78689676325672	1.08671494954617	5.88065083277250
600	1.02741326031740	−1.78689676325717	1.08671494979183	5.88065083423307
700	1.02741326030699	−1.78689676325563	1.08671494908700	5.88065083086592

This issue has been circumvented by taking $U_R = -1 + 10^{-10}$ to approximate MHD-Couette flow, which breaks antisymmetry above machine precision. This ensures that there is only one unstable eigenvalue, while having a negligible effect on the linear computations.

Extensive literature comparisons [63–65] were performed when Ref. [49] validated their method, for the $H = 0$ Posieuille flow problem. Testing the present formulation against this benchmark recovered the values for μ_1 and μ_2 to all six significant figures provided in Ref. [49]. The resolution required for higher H, Table III, demonstrates that the discretization for the linear stability problem yields acceptable results for the additional weakly nonlinear computations.

B. Results

Figure 11 depicts the weakly nonlinear behavior solely at the critical points (Fig. 3). Locally, the transition is subcritical ($\mu_2 > 0$) and the finite amplitude state can be reached ($\mu_1 > 0$) at all critical points, including along the $\mathrm{Re_c} \to \infty$ asymptotes. However, the magnitude of μ_2 directly quantifies the level of subcriticality of the transition. The variations of $\mathrm{Re}(\mu_2(H))$ are opposite to those of $\mathrm{Re_c}(H)$. As such, for the larger values of H, $\mathrm{Re}(\mu_2)$ scales with the Shercliff layer thickness and decreases as $\mathrm{Re}(\mu_2) \sim H^{-1/2}$. Near asymptotes where $\mathrm{Re_c}$ diverges, on the other hand, $\mathrm{Re}(\mu_2)$ increases sharply with H from $-\infty$. This is expected, since in this limit, any growth of finite amplitude takes place at a vanishingly small critical parameter $\mathrm{Re}/\mathrm{Re_c} - 1$. The by-product of this is that the saturation amplitude at which the perturbation is large enough for nonlinear effects to be important increases with H, as $|A|^2 \sim H^{5/2}$ for large H; see Fig. 11(c). However, to compare between H, a constant $\mathrm{Re}/\mathrm{Re_c}$ scaling of $|A|^2 \sim H^2$ is more appropriate, as $\mathrm{Re_c} \sim H^{1/2}$ for large H. Since, at constant Re, linear transient growth decreases at least as $H^{-1/2}$ [23], it is unlikely to provide a mechanism to support the growth of perturbations at large H. Thus, although subcritical bifurcations exist, they are unlikely to be obtained, given the lack of transient growth at subcritical Re.

$\mathrm{Re}(\mu_2)$ is depicted along neutral curves from the linear stability analysis in Fig. 12, for Shercliff, MHD-Couette, and mixed ($U_R = 0.85$) base flows. For Shercliff flow, at $H = 1$ and 10, $\mathrm{Re}(\mu_2)$ changes sign twice along the lower branch, so the bifurcation associated with modes on this branch is supercritical between these two points and subcritical elsewhere. At $H = 100$, the bifurcation becomes supercritical at a much higher Reynolds number (likely because the TS mode does not define the edge of the neutral curve there) and remains supercritical to the computed extent of the lower branch (to $\mathrm{Re} = 10^7$). Comparatively, for MHD-Couette flow, at $H = 15.11$ and 30, there is no supercritical region. At $H = 100$, a supercritical bifurcation appears along the lower branch, as at higher H, there is less sensitivity to the exact base flow profile. The mixed flow displays a clearer transition from subcritical to supercritical bifurcation with increasing H. At H near H^{∞} (0.601 and 1), the bifurcation is everywhere subcritical. At $H = 10$, a small region of supercritical bifurcation exists along the lower branch. By $H = 100$, this region of supercritical bifurcation is much larger and does not switch back to subcritical to the computed extent of the neutral curve ($\mathrm{Re} = 10^7$). However, the top branch always remains open to subcritical bifurcation.
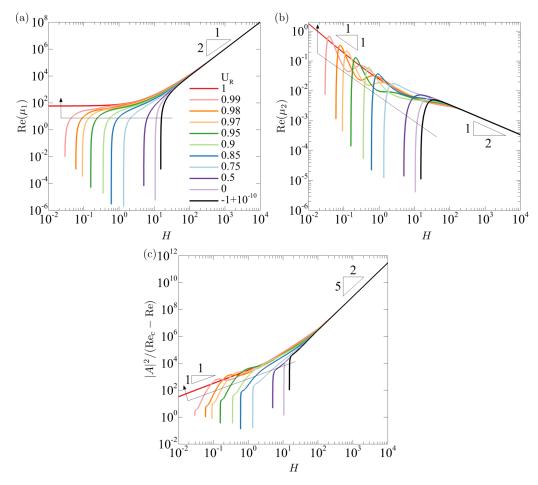
FIG. 11. Weakly nonlinear stability for various U_R at the critical points (recall Fig. 3). (a) Real part of linear growth rate correction coefficient. (b) Real part of first Landau coefficient. (c) Normalized amplitude. Arrows indicate increasing U_R. As $H \to \infty$, $|A|^2 = 29.8970 H^{5/2}(\mathrm{Re}_c - \mathrm{Re})$.

At large Reynolds numbers, the scalings $\alpha \sim \mathrm{Re}^{-1}$, $\mathrm{Re}(\mu_1) \sim \mathrm{Re}^{-1}$, and $\mathrm{Re}(\mu_2) \sim \mathrm{Re}^{-1}$ hold, and the phase speed asymptotes to a constant. Furthermore, as $\mathrm{Re}(\mu_1)(\mathrm{Re}_{\mathrm{marg}} - \mathrm{Re})$ always remains positive, the finite amplitude state can always be reached ($\mathrm{Re}_{\mathrm{marg}}$ is the Reynolds number on the neutral curve).

VII. DIRECT NUMERICAL SIMULATIONS

A. Formulation

Finally, we shall now assess whether transition to quasi-two-dimensional turbulence may actually take place under the full nonlinear dynamics, by performing direct numerical simulations (DNS) of Eqs. (1) and (2). Natural conditions are reproduced with white noise added in varying fraction $E_0(t = 0) = \int_{-1}^{1} \hat{u}^2 + \hat{v}^2 \, d\Omega / \int_{-1}^{1} U^2 \, d\Omega$, where Ω represents the computational domain. Periodic boundary conditions, $\boldsymbol{u}(x = 0) = \boldsymbol{u}(x = W)$ and $p(x = 0) = p(x = W)$, are applied at the downstream and upstream boundaries of a domain with length $W = 2\pi/\alpha_{\mathrm{max}}$ set to match the wave number that achieved maximal linear growth. The simulations typically exhibited a rapid drop in disturbance energy, followed by a linear phase of exponential growth, which is finally superseded
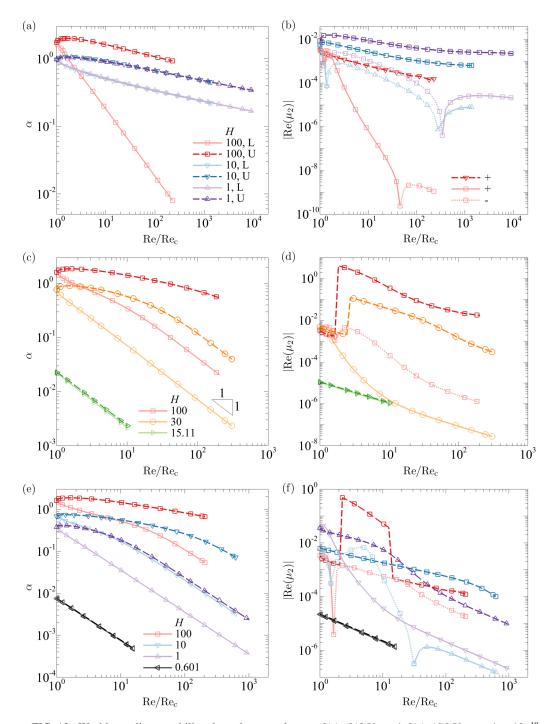
FIG. 12. Weakly nonlinear stability along the neutral curve. [(a), (b)] $U_R = 1$. [(c), (d)] $U_R = -1 + 10^{-10}$. [(e), (f)] $U_R = 0.85$. Neutrally stable wave numbers (left column) and real part of the first Landau coefficient (right column). Dotted lines denote where $\mathrm{Re}(\mu_2)$ was negative, indicating supercritical bifurcation. "L" and "U" denote the lower and upper branches of the neutral curve, respectively.

TABLE IV. DNS mesh resolution testing at $H = 100$ and $\mathrm{Re} = 10^6$, for Sercliff ($\mathrm{Re}_c = 4.40223 \times 10^5$; $\alpha_{\max} = 1.52813$ at $\mathrm{Re} = 10^6$) and MHD-Couette ($\mathrm{Re}_c = 4.87187 \times 10^5$; $\alpha_{\max} = 1.39883$ at $\mathrm{Re} = 10^6$) flow. The interpolant for each spectral element is order $N_p = 19$ and the time step is $\Delta t = 1.25 \times 10^{-3}$, as validated in Ref. [58]. The final resolution choices are in bold, where E_x and E_y represent the number of elements per unit length in x and y, respectively. The chosen resolution has roughly 650 elements and 6.25×10^5 degrees of freedom for these wave numbers.

E_x	E_y	$\sigma_{\Delta\max}, U_R = 1$	Error (%)	$\sigma_{\Delta\max}, U_R = -1$	Error (%)
3	12	$5.13119051 \times 10^{-3}$	2.236×10^{-1}	$3.92816302 \times 10^{-3}$	1.367×10^{-1}
6	12	$5.13138001 \times 10^{-3}$	2.273×10^{-1}	$3.92831007 \times 10^{-3}$	1.394×10^{-1}
3	**24**	$5.11994480 \times 10^{-3}$	3.959×10^{-3}	$3.93378788 \times 10^{-3}$	6.248×10^{-3}
6	24	$5.11998768 \times 10^{-3}$	4.797×10^{-3}	$3.93158203 \times 10^{-3}$	4.983×10^{-2}
LSA	LSA	$5.11974211 \times 10^{-3}$		$3.93354213 \times 10^{-3}$	

by nonlinear effects. The exponential growth rate $\sigma_{\max}$ from the linear growth regime is obtained by fitting the natural logarithm of $\int |v| \, d\Omega$ data over a few thousand time units. As $t_\Delta = t/(1 - U_{\min})$, the rescaled growth rate $\sigma_{\Delta\max} = \sigma_{\max}/(1 - U_{\min})$.

The random noise seeds (perturbations) are evolved with an in-house spectral element solver, which employs a third-order backward differencing scheme, with operator splitting, for time integration [66]. High-order Neumann pressure boundary conditions are imposed on impermeable walls to maintain third-order time accuracy [66]. The Cartesian domain is discretized with quadrilateral elements over which Gauss-Legendre-Lobatto nodes are placed ($N_p = 19$ nodes per element to take advantage of spectral convergence). Elements are uniformly distributed in both streamwise and transverse directions, with greater element compression in the wall-normal direction. At the highest H value simulated, at least 20 nodes reside within the Sercliff boundary layer. The solver, incorporating the SM82 friction term, has been previously introduced and validated [23,35,37,67].

Mesh validation results are provided in Table IV, comparing growth rates measured in the DNS against linear stability analysis (LSA) predictions. The agreement is excellent in the exponential growth (or decay) stages. Some additional comparisons at the chosen resolution (3 elements per unit length in x, 24 elements per unit height in y) can be found in Table V.

Fourier analysis is also performed at select instants in time, exploiting the streamwise periodicity of the domain. The absolute values of the Fourier coefficients $c_\kappa = |(1/N_f) \sum_{n=0}^{n=N_f-1} [\hat{u}^2(x_n) + \hat{v}^2(x_n)] e^{-2\pi i \kappa n/N_f}|$ were obtained using the discrete Fourier transform in MATLAB, where x_n represents the nth x location linearly spaced between $x_0 = 0$ and $x_{N_f} = W$, interpolating in the discretized domain when necessary, and taking $N_f = 10\,000$. A mean Fourier coefficient $\bar{c}_\kappa$ is obtained by averaging the coefficients obtained at 21 y values. A time-averaged mean Fourier coefficient $\langle \bar{c}_\kappa \rangle_t$ is also determined by averaging over approximately 20 time instants, for stages after the initial linear

TABLE V. Subcritical test cases for Sercliff flow at $H = 1$, with different levels of criticality at $E_0 = 10^{-2}$ (left) and with different values of E_0 at $\mathrm{Re}/\mathrm{Re}_c = 0.9$ (right).

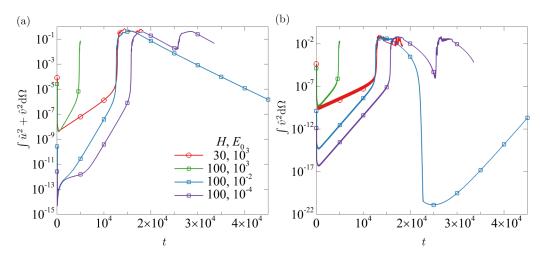|	$10^4 \sigma_{\Delta\max}$				$10^4 \sigma_{\Delta\max}$		
$\mathrm{Re}/\mathrm{Re}_c$	LSA	DNS	Error (%)	E_0	LSA	DNS	Error (%)
0.5	-76.4704	-76.4726	2.9×10^{-3}	10^2	-8.97961	-8.98230	3.0×10^{-2}
0.6	-52.0623	-52.0586	7.1×10^{-3}	10^{-0}	-8.97961	-8.98277	3.5×10^{-2}
0.7	-33.9759	-33.9774	4.4×10^{-3}	10^{-2}	-8.97961	-8.98232	3.0×10^{-2}
0.8	-20.0392	-20.0420	1.4×10^{-2}	10^{-4}	-8.97961	-8.98240	3.1×10^{-2}
0.9	-8.97961	-8.98232	3.0×10^{-2}	10^{-6}	-8.97961	-8.94802	3.5×10^{-1}

FIG. 13. Temporal evolution of perturbations initiated with random noise for MHD-Couette flow $(U_R = -1)$ at $\mathrm{Re}/\mathrm{Re}_c = 1.1$, and various $H > H^\infty$ and E_0. (a) $\int \hat{u}^2 + \hat{v}^2 \, d\Omega$. (b) $\int \hat{v}^2 \, d\Omega$.

and nonlinear growth. Note that although the number of sample points N_f is high, only κ up to about 100 to 200 are well resolved by the spatial discretization, depending on H.

B. Subcritical regime

The results for DNS at subcritical Reynolds numbers are collated in Table V. All initial seeds decayed exponentially, with excellent agreement to the LSA decay rates and without any observable linear transient growth. It appears that supercritical Reynolds numbers are required to induce nonlinear behavior and transitions to turbulence, if the initial field is random noise, more in line with a supercritical bifurcation. Thus, subcritical transitions may only be attainable for a small range of Reynolds numbers near Re_c. Subcritical tests of MHD-Couette flow for $H < H^\infty$ (for which $\alpha_{\max} \to 0$) were also simulated, with $W = 20\pi$ arbitrarily chosen; only monotonic decay was observed. Note that in all these cases, the transient growth optimals have wavelengths shorter than the domain length required to maximize linear growth, and are hence not excluded.

C. Supercritical regime

The energy growth for supercritical MHD-Couette flow (for $H > 15.102$) is shown in Fig. 13 and for supercritical Shercliff flow in Fig. 14. These are separated into growth in $\int \hat{u}^2 + \hat{v}^2 d\Omega$, to represent the total perturbation kinetic energy and to highlight the formation of streamwise independent structures, and growth in $\int \hat{v}^2 d\Omega$, which better isolates the growth or decay of the perturbation. The linear growth, nonlinear growth, and initial turbulent stages are very similar between the MHD-Couette and Shercliff flows. However, the relaminarization and decay stages are quite different. For MHD-Couette flow (Fig. 13), $\int \hat{v}^2 d\Omega$ displays clear re-excitations. The $H = 30$ and $H = 100$, $E_0 = 10^{-4}$ cases relaminarize, but are both quickly re-excited (very rapidly in the $H = 30$ case) while at high amplitudes, when nonlinearity still plays a role. The $H = 100$, $E_0 = 10^{-2}$ case cleanly decays to the floor, after which growth begins again, via the linear mechanism. This was not observed for Shercliff flow, with both (smaller E_0) $H = 30$ and $H = 100$ cases relaminarizing and rapidly monotonically decaying (the larger E_0 cases require exceedingly small time steps and as such their final behaviors remain unknown). The smaller E_0 case at $H = 30$ also relaminarizes and decays more rapidly than at $H = 100$, in spite of less Hartmann friction. Note that the energy in the Shercliff and MHD-Couette base flows at the same H differ, so it is not necessarily appropriate to compare the same E_0 between different base flows.
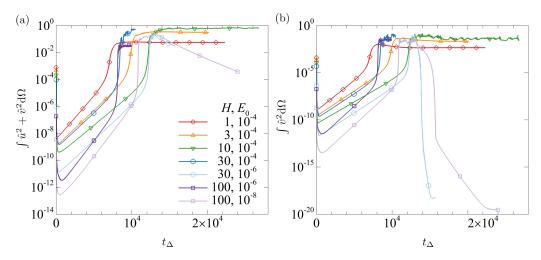
FIG. 14. Temporal evolution (rescaled time) of perturbations initiated with random noise for Shercliff flow ($U_R = 1$) at $Re/Re_c = 1.1$, and various H and E_0. (a) $\int \hat{u}^2 + \hat{v}^2 \, d\Omega$. (b) $\int \hat{v}^2 \, d\Omega$.

Computations of Shercliff flow reveal two interesting changes in behavior with decreasing H. Unlike the relaminarization and monotonic decay for $H \geqslant 30$, the $H = 3$ and $H = 10$ cases (with $E_0 = 10^{-4}$) maintain turbulent states. At $H = 3$ relaminarization again occurs, but the perturbation saturates to a stable finite amplitude state, rather than decaying. However, $H = 10$ maintains the turbulent state for the computed extent of the simulation, excepting two brief attempts at relaminarization, which are not stable, resulting in a return to turbulence. With further decreasing $H \leqslant 1$, no turbulent state is triggered by the linear and nonlinear growth, with only an eventual saturation to a stable finite amplitude state. This behavior echoes that discussed in Ref. [68], which observes that for all $Ha \geqslant 0$ a purely two-dimensional finite-amplitude state can be reach via evolution of an Orr mode formed of purely spanwise vortices (recall Sec. V B indicating that the transient Orr optimal was almost identical to the linear optimal). However, the addition of three-dimensional noise to the finite-amplitude state triggers (3D) turbulence at low Ha but destabilizes the finite-amplitude state at high Ha such that the solution decays back to the laminar base state, with only short-lived turbulence. It is presumed by Ref. [68] that this is due to nonlinear interactions feeding energy from 2D modes to 3D modes, which are then more rapidly dissipated at high Ha. Since this could not occur in these purely Q2D simulations, a different mechanism may be at play. References [41] and [42] argue that in hydrodynamic pipe flows, the flattening of the mean profile reduces turbulence production in the bulk, such that turbulence cannot be sustained. In the present configuration, production is almost solely due to $\hat{u}\hat{v}\partial U/\partial y$. The vanishing of this term in the core flow for $H \gtrsim 30$ may therefore explain why turbulence collapses in this parameter regime. Turbulence can still be re-excited as $\partial U/\partial y$ remains large near the wall. A possible explanation of the lack of transition at lower H then follows, as with reducing H, $\partial U/\partial y$ near the wall reduces, and so too production.

Figures 15 and 16 depict the y-averaged Fourier coefficients $\bar{c}_\kappa$ to compare the three different behaviors observed when $H \lesssim 1$ (high amplitude nonturbulent), $1 < H < 30$ (possibly long-lived turbulence), or $H \gtrsim 30$ (short-lived turbulence). Very few modes are energized throughout the linear region, with a rapid jump in the number of modes energized in the nonlinear growth phase. This is shown in any one of Figs. 15(a)–15(d), by comparing the fourth and fifth curves, which are closely spaced in time but which exhibit approximately an order of magnitude increase in the number of noticeably (relative to the floor) energized modes. For the $H = 1$ case, there is then no further change in the general form of the $\bar{c}_\kappa$ curves. However, for $H \geqslant 3$ even more modes continue to be energized, until the spectra are contaminated by under-resolution for $\kappa \gtrsim 200$. This is also shown in
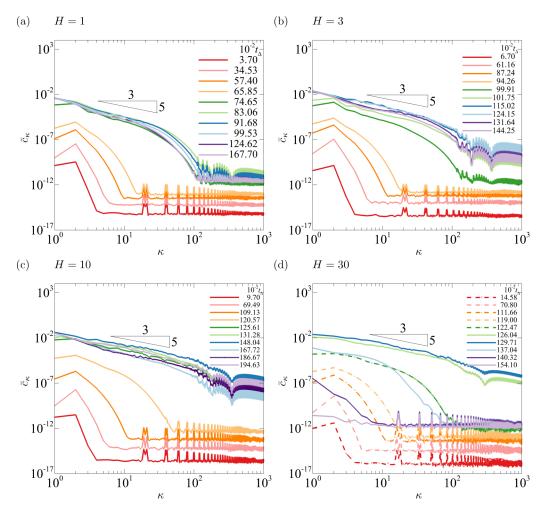
(a) $H = 1$

(b) $H = 3$

(c) $H = 10$

(d) $H = 30$

FIG. 15. Instantaneous (rescaled time) values of the y-averaged Fourier coefficients for $1 < \kappa < 10^3$, for Shercliff flow ($U_R = 1$) at $Re/Re_c = 1.1$; $E_0 = 10^{-4}$ for $H \leqslant 10$; $E_0 = 10^{-6}$ for $H = 30$.

Fig. 16(a) by comparing the time-averaged $\bar{c}_\kappa$, averaged only after the initial nonlinear growth. Only the cases with $H \geqslant 3$, for either Shercliff or MHD-Couette flow, demonstrate a range of wave numbers with perturbation energy with a $\kappa^{-5/3}$ dependence, which suggests the formation of an inertial subrange. There is also a sudden jump in the spectral floor for cases with $H \geqslant 3$ (also shown in Fig. 15, particularly at $H = 10$, comparing the curves at times $t_\Delta = 1.2057 \times 10^4$ and $t_\Delta = 1.2561 \times 10^4$). This is a good indication of a transition to turbulence, as the chaotic state with a limited number of excited modes becomes a turbulent state, where all available modes are excited. Conversely, the $H = 1$ data do not hold to the $\kappa^{-5/3}$ dependence for any distinct inertial subrange of κ, and a floor of low-energy modes is always observed, such that the low-H state never becomes turbulent. The $H = 30$ case in Fig. 15 also shows the resulting decay of the perturbation at larger times, with a rapid reduction in the number of energized modes, until the energy in all modes reaches the floor (the $-5/3$ trend holds briefly before this occurs). Figure 16(b) further supports the temporary turbulent nature of the flow in this $H = 30$ case, with the clear energization of all modes at $t_\Delta \approx 1.25 \times 10^4$, and the rapid decay of all but the zeroth mode (the streamwise independent structure) shortly thereafter, at $t_\Delta \approx 1.4 \times 10^4$. It also provides a different means of
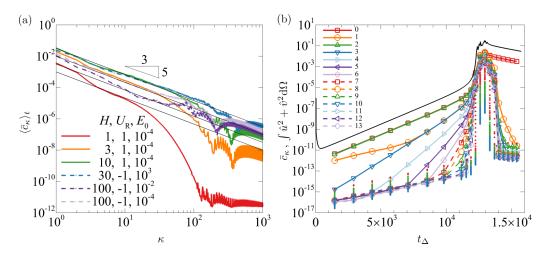
FIG. 16. (a) Time and y-averaged Fourier coefficients for $1 < \kappa < 10^3$, for both Shercliff and MHD-Couette flows at $\mathrm{Re}/\mathrm{Re}_c = 1.1$, for various H and E_0. The thin black lines show $\kappa^{-5/3}$ trends. $H \geqslant 30$ for Shercliff flow are not shown as the turbulence is short lived. (b) y-averaged Fourier coefficients as a function of rescaled time t_Δ for Shercliff flow at $\mathrm{Re}/\mathrm{Re}_c = 1.1$, $H = 30$, and $E_0 = 10^{-6}$. Modes $0 < \kappa < 13$ are as defined in the legend. Thereafter, every fifth mode is plotted, with $15 < \kappa < 100$ in red, $105 < \kappa < 1000$ in green, and $1005 < \kappa < 5000$ in blue. The black solid line is twice the perturbation energy, identical to that from Fig. 14(a).

viewing the energization of an increasing number of modes before noticeable nonlinear growth is achieved.

Representative flow fields are depicted for MHD-Couette flow in Fig. 17, at $H = 100$, $\mathrm{Re}/\mathrm{Re}_c = 1.1$, and $E_0 = 10^{-2}$ (energy growth depicted in Fig. 13). In the linear growth region, $2 \times 10^2 \lesssim t \lesssim 1.24 \times 10^4$, a pattern of similar structure to the linear stability eigenvector is observed in Fig. 17(a) (recall Fig. 5), although both the left and right running eigenvectors are observable in the nonlinear computation. Most of the energy in $\hat{u}^2$ is located where gradients in $\hat{v}$ are largest, i.e., very close to the walls. During the initial nonlinear growth period, $1.24 \times 10^4 \lesssim t \lesssim 1.26 \times 10^4$, the additional growth originates from the TS wave arching, as visible in the $\hat{v}$ field in Fig. 17(c), and the form of this dominant structure persists through the turbulent stage, $1.26 \times 10^4 \lesssim t \lesssim 1.78 \times 10^4$. Some underlying smaller scale features are also visible in Fig. 17(c). This dominant modulated TS wave can periodically break down and reform (as energy is driven to larger scales) throughout the turbulent stages. Linear transient optimals were found to experience a secondary nonlinear growth through the same mechanism in isolated exponential boundary layers [58], with a large-scale arched TS wave structure similarly persistent. The appearance of $\hat{u}$ also starkly changes with the nonlinear growth and transition to turbulence, with two elongated streamwise structures rapidly forming at each wall, which tend to reduce the local shear. These structures store perturbation energy, as shown by the slow decay of the zeroth mode in Fig. 16(b), and by comparing Figs. 13(a) and 13(b). After relaminarization, $1.78 \times 10^4 \lesssim t \lesssim 2.5 \times 10^4$, the TS wave flattens out [Fig. 17(e)], is pushed away from the high shear region (by the streamwise independent structure), and cleanly decays. As the Reynolds number is supercritical, the linear mode is re-excited from noise at the numerical floor.

However, the smaller turbulent scales in Fig. 17 are occluded by the dominance of the arched TS wave. Figure 18 depicts two snapshots revealing key flow features present in the smaller scales. In these snapshots, a high-pass filter has been applied to remove streamwise Fourier modes $|\kappa| \leqslant 9$ from the flows. Strongly localized jets emanating from the sidewalls entrain narrow shear layers, observable in the example at $H = 3$, while at $H = 100$ a myriad of smaller scale features are present.
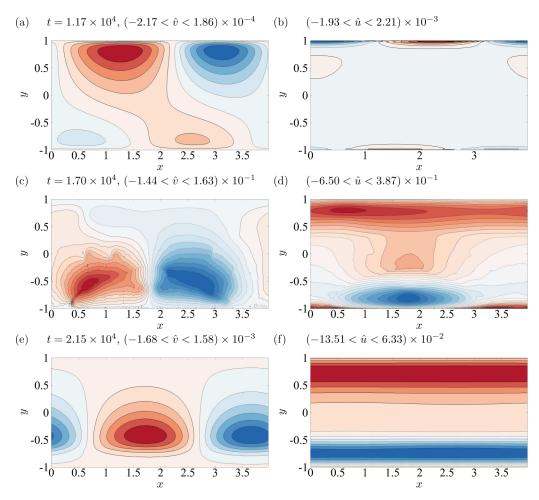
FIG. 17. Temporal snapshots of MHD-Couette flow at $\mathrm{Re}/\mathrm{Re_c} = 1.1$, $H = 100$, $E_0 = 10^{-2}$ (Fig. 13). Wall-normal velocity perturbation $\hat{v}$ (left); streamwise velocity perturbation $\hat{u}$ (right). Solid lines (red flooding) positive; dotted lines (blue flooding) negative. The linear TS wave evolves into an arched TS wave, leading to a turbulent state and the rapid growth of a streamwise independent structure. The TS wave then flattens out and relaminarization occurs.

VIII. CONCLUSIONS

This work examined the influence of the base flow in the scenario of transition to turbulence in a quasi-two-dimensional duct flow with a transverse magnetic field. The base flow is varied through the relative velocity of the two lateral walls. This is of particular importance in the context of recent developments in flow control, where turbulence is suppressed via the introduction of a friction effect to flatten the base flow [40,41,43]. Ideas along the same lines can be conversely applied to the promotion, rather than the suppression, of turbulence. Promoting turbulence to enhance heat transfer is indeed necessary for one of the motivations of this work: to assess the feasibility of dual-purpose liquid metal coolant ducts in magnetic confinement fusion reactors [1]. Fluid structures have a strong tendency to two dimensionalize within these ducts, which exhibit naturally flat base flows, due to the action of the Lorentz force. The linear stability of quasi-two-dimensional MHD-Couette-Shercliff base flows provided two key insights. First, the addition of any amount of antisymmetry to the base flow eventually leads to unconditional stability to infinitesimal perturbations at sufficiently
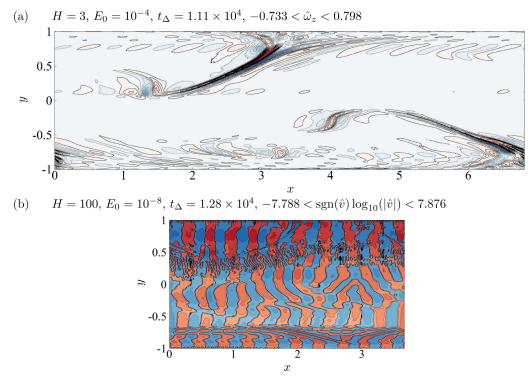
(a) $H = 3$, $E_0 = 10^{-4}$, $t_\Delta = 1.11 \times 10^4$, $-0.733 < \hat{\omega}_z < 0.798$

(b) $H = 100$, $E_0 = 10^{-8}$, $t_\Delta = 1.28 \times 10^4$, $-7.788 < \text{sgn}(\hat{v})\log_{10}(|\hat{v}|) < 7.876$

FIG. 18. Streamwise high-pass-filtered snapshots of Shercliff flow shortly after the transition to turbulence at $\text{Re}/\text{Re}_c = 1.1$. Streamwise Fourier coefficients of modes $|\kappa| \leqslant 9$ have been removed. Solid lines (red flooding) positive; dotted lines (blue flooding) negative.

low friction parameters H. The reason is that the antisymmetric part of the base flow drives the TS wave structures to destructively interfere, preventing growth. Conversely, an increasing friction parameter, beyond a critical value H^∞, flattens the central region of the base flow and isolates the wave structures at each wall, limiting their interaction, allowing growth to occur at finite critical Reynolds numbers. H^∞ increases with decreasing velocity of the bottom wall U_R, which controls the level of antisymmetry in the base flow (the top wall is at fixed velocity of unity). Only a symmetric, Shercliff base flow has finite Re_c for all nonzero H. Second, the critical parameters collapse to those of an isolated exponential boundary layer at high H, which occurs with noticeably lower imposed friction for increasingly antisymmetric base flow profiles. Antisymmetric profiles have a larger base flow velocity gradient at one wall than the other, leading the TS wave instability to preferentially form at only the one wall where the mean shear is largest. In such cases, friction need only keep the instability sufficiently far from the other wall to avoid any interference. This requires comparatively less friction than isolating two waves from one another (the greatest constructive interference thereby occurs in the symmetric Shercliff flow).

Conversely, the energetics of all Q2D MHD-Couette-Shercliff flows show little dependence on the degree of antisymmetry in the base flow. As such, the energetic Reynolds numbers are always finite. Furthermore, the transient growth of Q2D MHD-Couette-Shercliff flows is also not strongly dependent on the degree of antisymmetry in the base flow, with variations in growth between base flows only visible at $H \leqslant 10$. Destructive interference could explain the slight reduction in transient growth for more strongly antisymmetric base flows when H is small enough to permit interference. At larger friction parameters, $H \gtrsim 30$, transient growth is almost identical for all base flows. The growth attained is equivalent to that of an isolated exponential boundary layer [58] and

is increasingly damped with increasing H. Given that H would be of order 10^4 in a realistic fusion environment, linear transient growth may not be very relevant in their context.

The weakly nonlinear analysis also compounds the difficulties in promoting turbulence in realistic fusion environments, given the scaling of the equilibrium amplitude with $H^{5/2}$ for all base flows. However, the weakly nonlinear analysis still indicates the possibility of subcritical transitions for any H. Supercritical bifurcations are only found along the lower branch of the neutral curve and only for $H \gg H^{\infty}$. At lower friction parameters, for base flows with any degree of antisymmetry, the entire computed neutral curve indicates a subcritical bifurcation.

As the transient growth depicted little base flow dependence and has been previously analyzed in Ref. [58], direct numerical simulations target the exponential growth predicted by the linear stability analysis. There are two key findings. First, the relaminarization of turbulent states in symmetric Shercliff flows always occurred through a monotonic decay, while MHD-Couette flows experienced re-excitation to a turbulent state, in some cases at amplitudes where nonlinearity was relevant. Second, the magnitude of the friction parameter seemed to largely dictate the ability to trigger turbulence. At low $H \leqslant 1$, the linear and nonlinear growth led only to a saturated state, without turbulence. At intermediate $3 \leqslant H \leqslant 10$, a transition to turbulence was observed, and at $H = 10$ the turbulence state was maintained to the computed extent of simulations. Fourier analysis also indicated the presence of an inertial subrange, where the perturbation energy exhibited a wave number dependence of $\kappa^{-5/3}$. At higher $H \geqslant 30$ (the bound above which transient growth is equivalent to that of an isolated exponential boundary layer), although transition was observed, the turbulent state quickly collapsed. In all cases, the nonlinear growth and turbulence were dominated by a persistent large-scale arched TS wave. Streamwise independent structures also formed, which stored perturbation energy and which reduced the gradients in the boundary layers. Overall, the general features of the secondary nonlinear growth mirror that observed for the finite-amplitude linear transient optimals simulated in Ref. [58], where nonlinear growth is due to the arching of the conventional TS wave.

As a final word, the results of this paper indicate that it may be exceedingly difficult to obtain Q2D subcritical transitions with random, and even optimized, initial conditions. Future work may therefore be best focused on directly reducing $\mathrm{Re_c}$, permitting supercritical transitions at lower Reynolds numbers. Inflection points, introduced to the base flow with increasing antisymmetry, were not beneficial in this work due to their location. However, investigating the capabilities of inflection points within the boundary layers remains as a promising avenue for destabilizing Q2D flows (an ongoing work), which can be achieved through the use of time-periodic, rather than steady, wall motion.

[1] S. Smolentsev, R. Moreau, and M. Abdou, Characterization of key magnetohydrodynamic phenomena in PbLi flows for the US DCLL blanket, Fusion Eng. Des. **83**, 771 (2008).

[2] P. A. Davidson, *An Introduction to Magnetohydrodynamics* (Cambridge University Press, Cambridge, UK, 2001).

[3] J. Sommeria, Experimental study of the two–dimensional inverse energy cascade in a square box, J. Fluid Mech. **170**, 139 (1986).

[4] J. Sommeria, Electrically driven vortices in a strong magnetic field, J. Fluid Mech. **189**, 553 (1988).

[5] E. Lindborg, Can the atmospheric kinetic energy spectrum be explained by two-dimensional turbulence? J. Fluid Mech. **388**, 259 (1999).

[6] H. K. Moffatt, On the suppression of turbulence by a uniform magnetic field, J. Fluid Mech. **28**, 571 (1967).

[7] A. Alemany, R. Moreau, P. L. Sulem, and U. Frisch, Influence of an external magnetic field on homogeneous MHD turbulence, J. Méc. **18**, 277 (1979).

[8] Y. B. Kolesnikov and A. B. Tsinober, Experimental investigation of two-dimensional turbulence behind a grid, Fluid Dyn. **9**, 621 (1974).

[9] P. H. Roberts, *An Introduction to Magnetohydrodynamics* (Longmans, Green, New York, 1967).

[10] J. Sommeria and R. Moreau, Why, how, and when MHD turbulence becomes two-dimensional, J. Fluid Mech. **118**, 507 (1982).

[11] U. Schumann, Numerical simulation of the transition from three- to two-dimensional turbulence under a uniform magnetic field, J. Fluid Mech. **74**, 31 (1976).

[12] O. Zikanov and A. Thess, Direct numerical simulation of forced MHD turbulence at low magnetic Reynolds number, J. Fluid Mech. **358**, 299 (1998).

[13] A. Thess and O. Zikanov, Transition from two-dimensional to three-dimensional magnetohydrodynamic turbulence, J. Fluid Mech. **579**, 383 (2007).

[14] A. Pothérat and V. Dymkou, DNS of low-R_m MHD turbulence based on the least dissipative modes, J. Fluid Mech. **655**, 174 (2010).

[15] A. Pothérat and K. Kornet, The decay of wall-bounded MHD turbulence at low R_m, J. Fluid Mech. **783**, 605 (2015).

[16] N. T. Baker, A. Pothérat, L. Davoust, and F. Debray, Inverse and Direct Energy Cascades in Three-Dimensional Magnetohydrodynamic Turbulence at Low Magnetic Reynolds Number, Phys. Rev. Lett. **120**, 224502 (2018).

[17] A. Pothérat, Quasi-two-dimensional perturbations in duct flows under transverse magnetic field, Phys. Fluids **19**, 074104 (2007).

[18] R. Klein and A. Pothérat, Appearance of Three-Dimensionality in Wall Bounded MHD Flows, Phys. Rev. Lett. **104**, 034502 (2010).

[19] A. Pothérat and R. Klein, Why, how and when MHD turbulence at low R_m becomes three-dimensional, J. Fluid Mech. **761**, 168 (2014).

[20] P. Moresco and T. Alboussiére, Experimental study of the instability of the Hartmann layer, J. Fluid Mech. **504**, 167 (2004).

[21] D. Krasnov, O. Zikanov, M. Rossi, and T. Boeck, Optimal linear growth in magnetohydrodynamic duct flow, J. Fluid Mech. **653**, 273 (2010).

[22] D. Krasnov, O. Zikanov, and T. Boeck, Numerical study of magnetohydrodynamic duct flow at high Reynolds and Hartmann numbers, J. Fluid Mech. **704**, 421 (2012).

[23] O. G. W. Cassels, T. Vo, A. Pothérat, and G. J. Sheard, From three-dimensional to quasi-two-dimensional: Transient growth in magnetohydrodynamic duct flows, J. Fluid Mech. **861**, 382 (2019).

[24] L. Bühler, Instabilities in quasi-two-dimensional magnetohydrodynamic flows, J. Fluid Mech. **326**, 125 (1996).

[25] A. Pothérat, J. Sommeria, and R. Moreau, An effective two-dimensional model for MHD flows with a transverse magnetic field, J. Fluid Mech. **424**, 75 (2000).

[26] A. Pothérat and J. Schweitzer, A shallow water model for magnetohydrodynamic flows with turbulent Hartmann layers, Phys. Fluids **23**, 055108 (2011).

[27] J. Pedlosky, *Geophysical Fluid Dynamics* (Springer-Verlag, Berlin, 1987).

[28] J. Young, S. Smolentsev, and M. Abdou, Study of instabilities in a quasi-2D MHD duct flow with an inflectional velocity profile, Fusion Eng. Des. **89**, 1163 (2014).

[29] A. Thess, Instabilities in two–dimensional spatially periodic flows. Part I: Kolmogorov flow, Phys. Fluids A **4**, 1385 (1992).

[30] A. Thess, Instabilities in two-dimensional periodic flows. Part III: Square eddy lattice, Phys. Fluids A **4**, 1396 (1992).

[31] A. Thess, Instabilities in two-dimensional periodic flows. Part III: Inviscid triangular lattice, Phys. Fluids A **5**, 335 (1993).

[32] A. Pothérat, J. Sommeria, and R. Moreau, Numerical simulations of an effective two-dimensional model for flows with a transverse magnetic field, J. Fluid Mech. **534**, 115 (2005).

[33] V. Dousset and A. Pothérat, Numerical simulations of a cylinder wake under a strong axial magnetic field, Phys. Fluids **20**, 017104 (2008).

[34] W. K. Hussam, M. C. Thompson, and G. J. Sheard, Enhancing heat transfer in a high Hartmann number magnetohydrodynamic channel flow via torsional oscillation of a cylindrical obstacle, Phys. Fluids **24**, 113601 (2012).

[35] W. K. Hussam, M. C. Thompson, and G. J. Sheard, Optimal transient disturbances behind a circular cylinder in a quasi-two-dimensional magnetohydodynamic duct flow, Phys. Fluids **24**, 024105 (2012).

[36] A. H. A. Hamid, W. K. Hussam, A. Pothérat, and G. J. Sheard, Spatial evolution of a quasi-two-dimensional Karman vortex street subjected to a strong uniform magnetic field, Phys. Fluids **27**, 053602 (2015).

[37] O. G. W. Cassels, W. K. Hussam, and G. J. Sheard, Heat transfer enhancement using rectangular vortex promoters in confined quasi-two-dimensional magnetohydrodynamic flows, Int. J. Heat Mass Transfer **93**, 186 (2016).

[38] T. Vo, A. Pothérat, and G. J. Sheard, Linear stability of horizontal, laminar fully developed, quasi-two-dimensional liquid metal duct flow under a transverse magnetic field heated from below, Phys. Rev. Fluids **2**, 033902 (2017).

[39] J. C. R. Hunt and J. A. Shercliff, Magnetohydrodynamics at high Hartmann number, Annu. Rev. Fluid Mech. **3**, 37 (1971).

[40] E. Marensi, A. P. Willis, and R. R. Kerswell, Stabilisation and drag reduction of pipe flows by flattening the base profile, J. Fluid Mech. **863**, 850 (2019).

[41] J. Kühnen, B. Song, D. Scarselli, N. B. Budanur, M. Riedl, A. P. Willis, M. Avila, and B. Hof, Destabilizing turbulence in pipe flow, Nat. Phys. **14**, 386 (2018).

[42] N. B. Budanur, E. Marensi, A. P. Willis, and B. Hof, Upper edge of chaos and the energetics of transition in pipe flow, Phys. Rev. Fluids **5**, 023903 (2020).

[43] B. Hof, A. de Lozar, M. Avila, X. Tu, and T. M. Schneider, Eliminating turbulence in spatially intermittent flows, Science **327**, 1491 (2010).

[44] P. J. Schmid and D. S. Henningson, *Stability and Transition in Shear Flows* (Springer-Verlag, New York, 2001).

[45] J. A. C. Weideman and S. C. Reddy, A MATLAB differentiation matrix suite, ACM Trans. Math. Software **26**, 465 (2001).

[46] L. N. Trefethen, *Spectral Methods in MATLAB* (Society for Industrial and Applied Mathematics, Philadelphia, 2000).

[47] J. Hagan and J. Priede, Capacitance matrix technique for avoiding spurious eigenmodes in the solution of hydrodynamic stability problems by Chebyshev collocation method, J. Comput. Phys. **238**, 210 (2013).

[48] T. Kakutani, The hydromagnetic stability of the modified plane Couette flow in the presence of a transverse magnetic field, J. Phys. Soc. Jpn. **19**, 1041 (1964).

[49] J. Hagan and J. Priede, Weakly nonlinear stability analysis of magnetohydrodynamic channel flow using an efficient numerical approach, Phys. Fluids **25**, 124108 (2013).

[50] M. Takashima, The stability of the modified plane Couette flow in the presence of a transverse magnetic field, Fluid Dyn. Res. **22**, 105 (1998).

[51] R. J. Lingwood and T. Alboussière, On the stability of the Hartmann layer, Phys. Fluids **11**, 2058 (1999).

[52] C. Airiau and M. Castets, On the amplification of small disturbances in a channel flow with a normal magnetic field, Phys. Fluids **16**, 2991 (2004).

[53] P. G. Drazin and W. H. Reid, *Hydrodynamic Stability* (Cambridge University Press, Cambridge, UK, 2004).

[54] D. D. Joseph, *Stability of Fluid Motions I* (Springer-Verlag, Berlin, 1976).

[55] D. Barkley, H. M. Blackburn, and S. J. Sherwin, Direct optimal growth analysis for timesteppers, Int. J. Numer. Methods Fluids **57**, 1435 (2008).

[56] E. Hairer, S. P. Nørsett, and G. Wanner, *Solving Ordinary Differential Equations I: Nonstiff Problems* (Springer-Verlag, Berlin, 1993).

[57] H. M. Blackburn, D. Barkley, and S. J. Sherwin, Convective instability and transient growth in flow over a backward-facing step, J. Fluid Mech. **603**, 271 (2008).

[58] C. J. Camobreco, A. Pothérat, and G. J. Sheard, Subcritical route to turbulence via the Orr mechanism in a quasi-two-dimensional boundary layer, Phys. Rev. Fluids **5**, 113902 (2020).

[59] S. C. Reddy, P. J. Schmidt, and D. S. Henningson, Pseudospectra of the Orr-Sommerfeld operator, SIAM J. Appl. Math. **53**, 15 (1993).

[60] S. C. Reddy and D. S. Henningson, Energy growth in viscous channel flows, J. Fluid Mech. **252**, 209 (1993).

[61] L. N. Trefethen, A. E. Trefethen, S. C. Reddy, and T. A. Driscoll, Hydrodynamic stability without eigenvalues, Science **261**, 578 (1993).

[62] K. M. Butler and B. F. Farrell, Three-dimensional optimal perturbations in viscous shear flow, Phys. Fluids A **4**, 1637 (1992).

[63] P. K. Sen and D. Venkateswarlu, On the stability of plane Poiseuille flow to finite-amplitude disturbances, considering the higher-order Landau coefficients, J. Fluid Mech. **133**, 179 (1983).

[64] W. C. Reynolds and M. C. Potter, Finite-amplitude instability of parallel shear flows, J. Fluid Mech. **27**, 465 (1967).

[65] K. Stewartson and J. T. Stuart, A non-linear instability theory for a wave system in plane Poiseuille flow, J. Fluid Mech. **48**, 529 (1971).

[66] G. E. Karniadakis and S. J. Sherwin, *Spectral/HP Element Methods for Computational Fluid Dynamics* (Oxford University Press, Oxford, UK, 2005).

[67] G. J. Sheard, M. J. Fitzgerald, and K. Ryan, Cylinders with square cross-section: Wake instabilities with incidence angle variation, J. Fluid Mech. **630**, 43 (2009).

[68] D. Krasnov, M. Rossi, O. Zikanov, and T. Boeck, Optimal growth and transition to turbulence in channel flow with spanwise magnetic field, J. Fluid Mech. **596**, 73 (2008).